INL/LTD-17-43900-Revision-0

OECD/NEA COUPLED NEUTRONIC/THERMAL FLUIDS BENCHMARK

October 2020

Gerhard Strydom, Javier Ortensi

Changing the World's Energy Future

INL is a U.S. Department of Energy National Laboratory operated by Battelle Energy Alliance, LLC

INL/LTD-17-43900-Revision-0

OECD/NEA COUPLED NEUTRONIC/THERMAL FLUIDS BENCHMARK

Gerhard Strydom, Javier Ortensi

October 2020

Idaho National Laboratory
Idaho Falls, Idaho 83415

http://www.inl.gov

Prepared for the
U.S. Department of Energy
Under DOE Idaho Operations Office
Contract Unknown

Nuclear Science
NEA/NSC/R(2019)6
February 2020
www.oecd-nea.org

Coupled Neutronic/Thermal-Fluid Benchmark of the MHTGR-350 MW Core Design: Results for the Lattice Physics Exercises

OECD
BETTER POLICIES FOR BETTER LIVES

NEA
NUCLEAR ENERGY AGENCY

Nuclear Energy Agency

NEA/NSC/R(2019)6

Unclassified

English text only

16 October 2020

NUCLEAR ENERGY AGENCY
NUCLEAR SCIENCE COMMITTEE

Cancels & replaces the same document of 3 March 2020

Coupled Neutronic/Thermal-Fluid Benchmark of the MHTGR-350 MW Core Design: Results for the Lattice Physics Exercises

This document is available as PDF only.

JT03466982

ORGANISATION FOR ECONOMIC CO-OPERATION AND DEVELOPMENT

The OECD is a unique forum where the governments of 36 democracies work together to address the economic, social and environmental challenges of globalisation. The OECD is also at the forefront of efforts to understand and to help governments respond to new developments and concerns, such as corporate governance, the information economy and the challenges of an ageing population. The Organisation provides a setting where governments can compare policy experiences, seek answers to common problems, identify good practice and work to co-ordinate domestic and international policies.

The OECD member countries are: Australia, Austria, Belgium, Canada, Chile, the Czech Republic, Denmark, Estonia, Finland, France, Germany, Greece, Hungary, Iceland, Ireland, Israel, Italy, Japan, Korea, Latvia, Lithuania, Luxembourg, Mexico, the Netherlands, New Zealand, Norway, Poland, Portugal, the Slovak Republic, Slovenia, Spain, Sweden, Switzerland, Turkey, the United Kingdom and the United States. The European Commission takes part in the work of the OECD.

OECD Publishing disseminates widely the results of the Organisation's statistics gathering and research on economic, social and environmental issues, as well as the conventions, guidelines and standards agreed by its members.

NUCLEAR ENERGY AGENCY

The OECD Nuclear Energy Agency (NEA) was established on 1 February 1958. Current NEA membership consists of 33 countries: Argentina, Australia, Austria, Belgium, Canada, the Czech Republic, Denmark, Finland, France, Germany, Greece, Hungary, Iceland, Ireland, Italy, Japan, Korea, Luxembourg, Mexico, the Netherlands, Norway, Poland, Portugal, Romania, Russia, the Slovak Republic, Slovenia, Spain, Sweden, Switzerland, Turkey, the United Kingdom and the United States. The European Commission and the International Atomic Energy Agency also take part in the work of the Agency.

The mission of the NEA is:

– to assist its member countries in maintaining and further developing, through international co-operation, the scientific, technological and legal bases required for a safe, environmentally sound and economical use of nuclear energy for peaceful purposes;

– to provide authoritative assessments and to forge common understandings on key issues as input to government decisions on nuclear energy policy and to broader OECD analyses in areas such as energy and the sustainable development of low-carbon economies.

Specific areas of competence of the NEA include the safety and regulation of nuclear activities, radioactive waste management and decommissioning, radiological protection, nuclear science, economic and technical analyses of the nuclear fuel cycle, nuclear law and liability, and public information. The NEA Data Bank provides nuclear data and computer program services for participating countries.

Foreword

Under the auspices of the Nuclear Energy Agency (NEA) Nuclear Science Committee (NSC), the Working Party on Scientific Issues of Reactor Systems (WPRS) has been established to study the physics of present and future nuclear power systems. The Generation IV International Forum has highlighted helium-cooled very high temperature gas reactors as a key technology with the potential to improve the competiveness of nuclear energy. Developing tools and methods to support this technology is seen as a priority by NEA member countries.

Accurate modelling and simulation tools for neutronics calculations are a key element needed to design high temperature gas-cooled reactors. Uncertainties in modelling and simulation can have significant safety and economic implications.

The purpose of this prismatic High Temperature Reactor (HTR) benchmark is to provide a solution set that can be used in future code benchmarking and to better understand the effects induced by the presence of burnable poisons and different neighbours in a super-cell arrangement. This configuration is particularly representative of the fuel in the MHTGR-350 reactor core. Solutions from two Monte Carlo and two deterministic codes have been analysed. Means and standard deviations are provided at beginning, middle, and end of life for a variety of parameters. The report includes multiplication factors, detailed block-power distributions, spectral parameters, two-group cross-sections, as well as actinide and fission-product inventories. The analysis is focused on two spatial locations with very different neutron-energy spectra. The results from the benchmark indicate that there is very good agreement between participants in the integral parameters, but that significant differences appear in the concentrations of various isotopes. Some are due to the use of the reactivity physical transformation methodology, which captures reactivity effects very well, but does not produce the correct self-shielding in ^{238}U. This leads to poor predictions of the ^{239}Pu and other higher actinides.

Table of contents

List of figures

List of tables

List of abbreviations and acronyms

BOL	Beginning of life
BP	Burnable poison
EOL	End of life
FBP	Fixed burnable poison
GRS	Gesellschaft für Anlagen- und Reaktorsicherheit (Germany)
GWd	Gigawatt-day
HTGR	High-temperature gas reactor
HTR	High-temperature reactor
INL	Idaho National Laboratory (United States)
KAERI	Korea Atomic Energy Research Institute
MC	Monte Carlo
MG	Multi-group
MHTGR	Modular high-temperature gas-cooled reactor
MOC	Method of characteristics
MOL	Middle of life
MTIHM	Metric tonne of initial heavy metal
MTU	Metric tonne of uranium (equivalent to MTIHM)
NEA	Nuclear Energy Agency
PCM	Per cent mille (1/1 000 of a per cent of the reactivity)
PMR	Prismatic modular reactor
RIT	Resonance integral tabulation
RPT	Reactivity physical transformation
RSD	Relative standard deviation
SD	Standard deviation

1. Introduction

The depletion of nuclear fuel is a problem that is dependent on the neutron-flux distribution and the probability of neutron interactions, i.e. the cross-sections. In most thermal reactors, as in the prismatic high-temperature gas reactor (HTGR), the primary neutron absorption reactions that dominate the depletion of fuel are thermal-neutron fission and radiative capture. The spatial and energy distribution of neutron flux play an important role, not only in the computation of the reaction rates but also in the determination of cross-sections, whereas their angular dependence is less prominent. In the HTGR, changes in neutron flux span large domains because of the long mean free paths of neutrons and the low moderating power of graphite, which effectively produces a neutron behaviour characterised by long neutron migration lengths, on the order of 70 cm. Changes to neutron-flux spatial and energy distribution transpire for various reasons, which include the isotopic changes in fuel during depletion, proximity of reflectors, proximity of other fuel, and the presence of burnable poisons and or control rods.

The purpose of this prismatic high-temperature reactor (HTR) benchmark is to 1) provide a solution set that can be used in future code benchmarking; and 2) understand better the effects induced by the presence of burnable poisons and different neighbours in a super-cell (larger core domain) configuration. This configuration was specifically chosen because it is representative of a large portion of the fuel in the modular high-temperature gas-cooled reactor (MHTGR)-350 [1] core design. The presence of both a reflector and burned fuel near a fresh-fuel block creates a particularly interesting and challenging problem, even for computer codes considered state-of-the-art.

2. Description of lattice physics exercises

The depletion benchmark is intended to examine variation in lattice calculations between benchmark participants. The calculations are performed on a super-cell arrangement with dimensions given in [1] and a geometric representation shown in Figure 1. Three major regions are defined: 1) central fresh-fuel region (depleting region); 2) homogenised burned-fuel region at the bottom (non-depleting region); and 3) reflector region at the top (non-depleting region). Note the presence of six fixed burnable poisons (FBPs), one in each corner of the central block.

Two distinct exercises are included. The first exercise aims at establishing the accuracy of the self-shielding (if necessary) and flux solution methods without depletion and a standard benchmarking temperature of 293.6 K. The second exercise adds the depletion of the centre fuel region at 1 200.0 K. In each exercise, two cases are studied: without and with burnable poisons. Therefore, the first exercise entails cases 1a) initial steady state in cold conditions without burnable poisons and 1b) initial steady state in cold conditions with burnable poisons. Therefore, the second exercise entails cases 2a) depletion in hot conditions without burnable poisons and 2b) depletion in hot conditions with burnable poisons.

Figure 1: Graphical representation of the super-cell

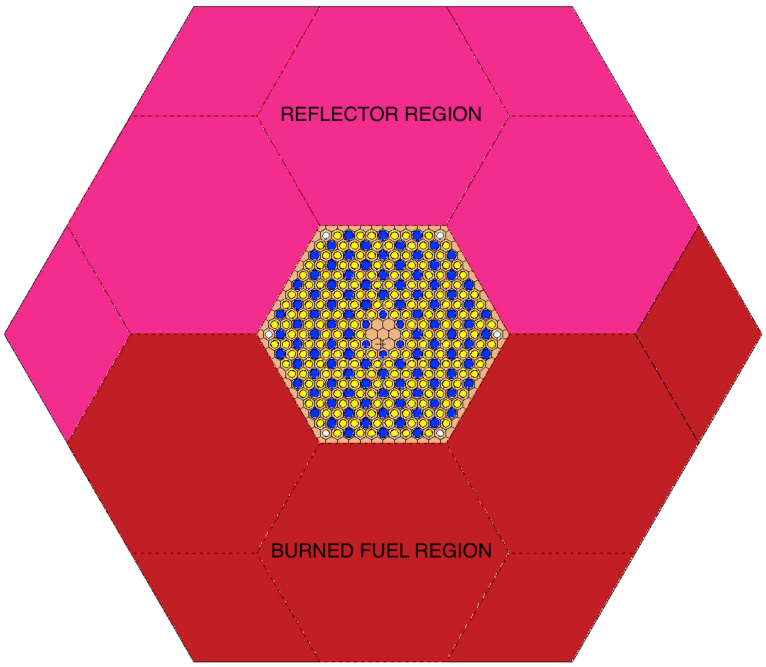

Source: OECD/NEA, 2020.

The depletion is performed at a constant power, assuming continuous burn-up with no downtime, as indicated in Table III-2 of Duderstadt. It should be noted that only the central fresh-fuel block is depleted. The depletion calculations are to be performed without a critical-spectrum correction. The reporting regions are shown in Figure 2.

Figure 2: Reporting locations for the depletion calculation

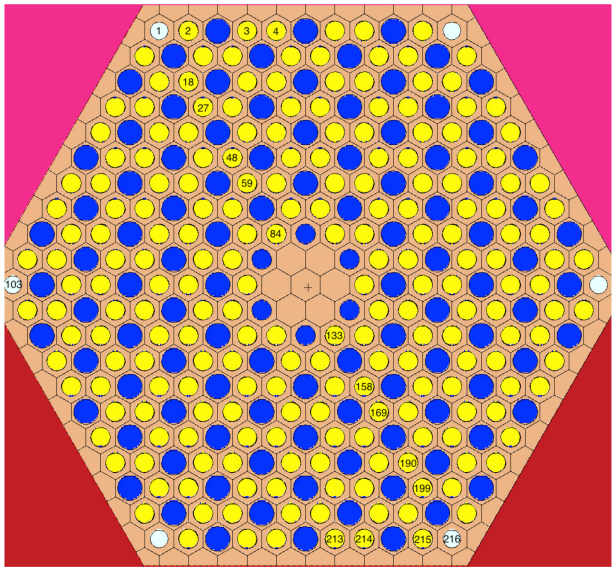

Source: OECD/NEA, 2020.

3. Participants and computer codes

Three organisations participated in this benchmark, and solutions from four computer codes were submitted for the benchmark. The list of participants and computer codes is shown in Table 1. Details on the computer code methods and neutron libraries are included in Table 2. The double heterogeneous nature of both fuel and burnable poison play an important role in these calculations and is likely to be a major sources of uncertainty. The two Monte Carlo codes use an explicit random distribution of particles. DeCART relies on a stochastic medium approach [3,4] and the reactivity physical transformation (RPT) method [5,6] was employed with HELIOS-2. It is important to note that the RPT is not a HELIOS methodology, but more of an analysis approximation due to the absence of a double heterogeneity treatment in the collision probability solver of HELIOS. The double heterogeneity solver in HELIOS is currently only available with the MOC solver, but unfortunately, this solver has yet to be optimised and tested for HTR calculations.

Table 1: List of participants and transport codes used

Organisation label	Organisation	Codes	Country
INL	Idaho National Laboratory	SERPENT v2	United States
KAERI	Korea Atomic Energy Research Institute	DeCART	Korea
		McCARD	
GRS	Gesellschaft für Anlagen- und Reaktorsicherheit	HELIOS-2	Germany

Source: OECD/NEA, 2020.

Energy self-shielding calculations in the deterministic codes use a mixture of subgroup methodology [7] and direct resonance integral tabulation (RIT). In the Monte Carlo method, energy and spatial self-shielding are inherent in the method. Energy self-shielding is quite important in HTRs because it directly affects the production of higher actinides via ^{238}U neutron radiative capture.

Table 2: Codes and methodologies

Codes	Double heterogeneity treatment	Library energy groups	Library nuclides	Resonance self-shielding method	Spatial flux solution method	Depletion solver
Serpent v2	Explicit random	N/A	1343	N/A	MC	CRAM
DeCART	Stochastic medium	190*	327	Subgroup and RIT	MOC	Krylov subspace method
McCARD	Explicit random	N/A	1297	N/A	MC	matrix exponential method via Taylor series
HELIOS-2	Reactivity physical transformation (RPT)	335*	241	Subgroup and RIT	CCCP	4th order Runge-Kutta

*Specialised library for VHTR

Source: OECD/NEA, 2020.

4. Analysis method

The mean value (μ) was calculated for various parameters of interest. The associated standard deviation (SD) and the relative standard deviation (RSD) of the calculated parameters were also determined according to the following formulae, where N is the number of participants:

$$\mu = \frac{1}{N}\sum_{i=1}^{N} x_i$$

$$SD = \sqrt{\frac{1}{N}\sum_{i=1}^{N}(x_i - \mu)^2}$$

$$RSD = 100\frac{SD}{\mu}$$

The RSD indicates the degree of consistency between the results provided by participants: a small RSD for a given parameter indicates consistency among the various codes and data used, whereas a large RSD indicates a poor agreement.

For this benchmark, it was assumed that a good agreement between participants has been obtained when the RSD is less than the maximum shown in Table 3. Conversely, if the quantities under comparison (e.g. eigenvalue, power, and flux) have an RSD larger than the one listed in the table, it was considered to indicate poor agreement between participants' results. It should be noted that a low RSD does not mean that all the participants calculated the correct value, merely that they each calculated a similar value.

Table 3: Maximum relative standard deviation for various parameters

Parameter	Maximum RSD
Multiplication factor (k)	0.2%
Peaking factors	2.0%
Cross-sections (fast)	3.0%
Cross-sections (thermal)	1.0%

Source: OECD/NEA, 2020.

The peaking factor at each i^{th} fuel compact in the central fuel block is defined as the ratio of the power in the i^{th} fuel compact and the average power in the block and expressed as:

$$f_i = \frac{P_i}{\frac{1}{I}\sum_{i=1}^{I} P_i}$$

where I is the total number of fuel pins and P is the pin power.

The normalisation of the flux per unit lethargy follows the specification in the benchmark document [2]. The fast-to-thermal energy boundary was set high (4.95 eV) in the benchmark specification; therefore, the upscattering is set to zero because the cross-section values are very small and the deviations very high. It is important to note that deterministic codes rely on a multi-group (MG) library that might not include this precise energy threshold; thus, the threshold used might be slightly lower or higher than prescribed in the specification.

In this report beginning of life (BOL), middle of life (MOL) and end of life (EOL) are defined as points at 0, 60 and 120 GWd/MTU. Note: 1 GWd/MTU = 1 MWd/kgU. In the super-cell configuration, two clearly delineated neutron-spectral zones exists: 1) a soft or thermal zone near the reflector; and 2) a hard or fast spectral zone near the burned fuel. The words "soft" and "thermal" are used interchangeably throughout the document. The same applies to the terms "hard" and "fast," when referring to the neutron energy spectrum.

Exercise 1 results

The multiplication factors for cases 1a and 1b are included in Table 4. There is good agreement between the various participants with standard deviations below 100 pcm for both cases, with and without burnable poison (BP). The mean BP worth obtained when replacing graphite with B_4C in the BP region is -6.77%.

Table 4: Multiplication factors for cases 1a and 1b

CODE	k(1a)	k(1b)	Δρ
HELIOS	1.23622	1.14047	-6.79%
DeCART	1.23686	1.14173	-6.74%
McCARD	1.23519	1.13945	-6.80%
SERPENT	1.23571	1.14056	-6.75%
Mean (μ)	1.23600	1.14055	-6.77%
SD [pcm]	61.81	80.76	27.34

Source: OECD/NEA, 2020.

The mean value of the peaking factors and associated RSD for case 1a are shown in Figure 3. The results show good agreement among the various participants, with a maximum RSD of 2.15%. A significant gradient in the peaking factor is visible across the central fuel block, with a maximum f_i of 2.25 near the reflector and minimum f_i of 0.57 near the burned fuel. This is a well-known phenomenon because the presence of the reflector tends to further thermalise the neutron energy spectrum, whereas the presence of a burned fuel region tends to harden it.

To further study these spectral changes, a plot of the flux per unit lethargy from Serpent in various compact positions across the block is included in Figure 4. The compact position is consistent with Figure 2, with compact 2 near the reflector and 215 near the burned-fuel region. The plot shows a significant change in the thermal peak in the first half of the fuel block, a factor of three, while the other half, facing the burned fuel, experiences small changes. In the latter region, the changes in the magnitude in the fast energy domain are magnified due to the division of the flux over the lethargy bin.

Figure 3: Mean (a) value and RSD (b) of the peaking factors for case 1a

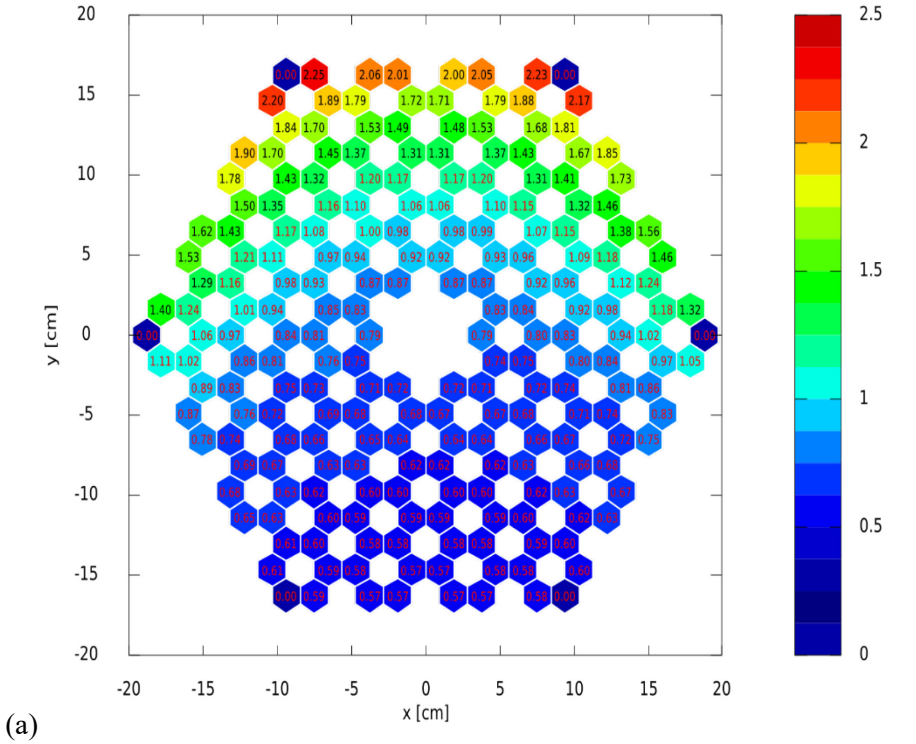

(a)

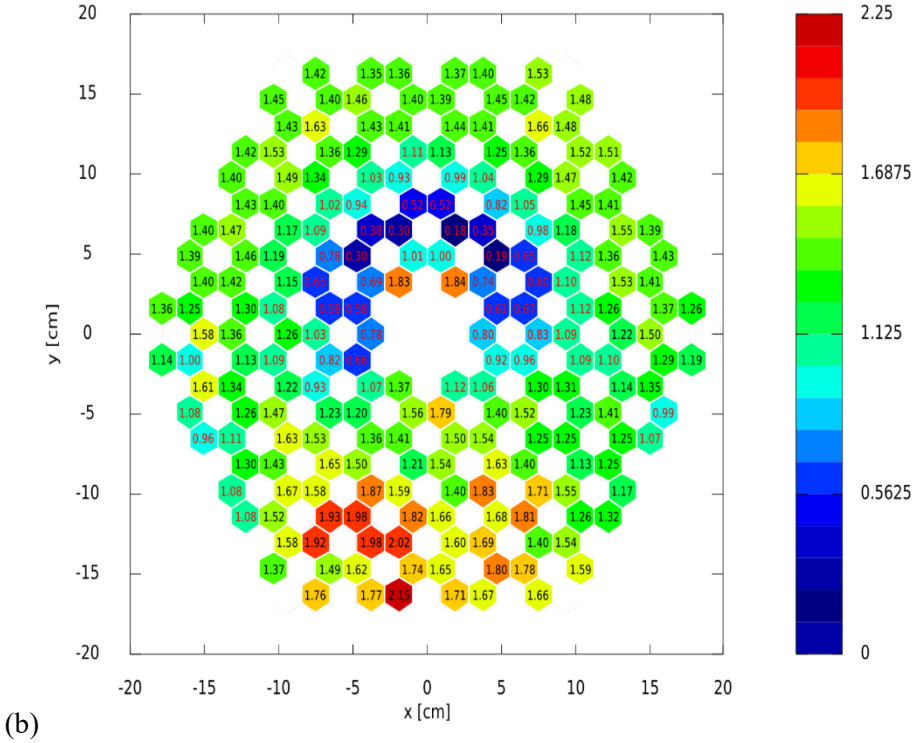

(b)

Source: OECD/NEA, 2020.

Figure 4: Neutron flux per lethargy for case 1a

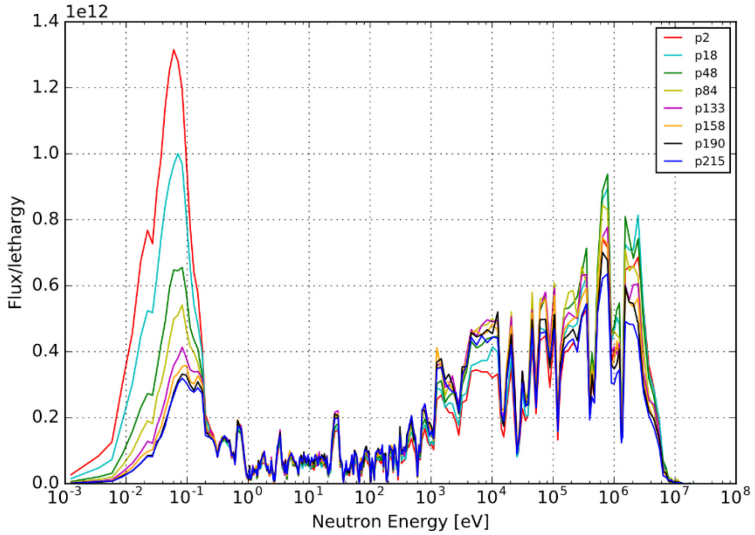

Source: OECD/NEA, 2020.

Values of the spectral indices were only provided by the two Monte Carlo codes, Serpent and McCARD, and are shown in Figure 5. The variation in the neutron energy spectrum is apparent in the results of the fast to thermal ^{238}U capture, ρ_{238}, which is a factor of 4 times higher near the once-burned fuel region. This number is consistent with the change in the ratio of fast versus thermal ^{235}U fission, δ_{235}. The c/f_{235} indicates that for each fission in ^{235}U, there will be roughly twice as many ^{238}U capture events near the burned-fuel region closer to the reflector. Finally, the ratio of ^{238}U to ^{235}U fissions is also twice as large near the burned-fuel region.

The mean value of the peaking factors and associated RSD for case 1b are shown in Figure 6. The results show good agreement between the various participants, with a maximum RSD of 2.01%. With the addition of the BPs, the spectrum hardens across the central fuel block and reduces the peaking by an average 5% on the reflector side, increases by a similar value on the burned-fuel side. The gradient of the former region is substantially steeper than that of the latter, but it is significantly improved over the initial gradient without BP. The maximum peak is reduced by 15%, and all peaking factors remain just below 2. The flux per unit lethargy in the presence of BPs in Figure 7 clearly indicates that the magnitude of the thermal peaks has been reduced, but also the difference between the various peaks near the centre of the fuel block has increased.

Figure 5: Spectral indices for case 1a

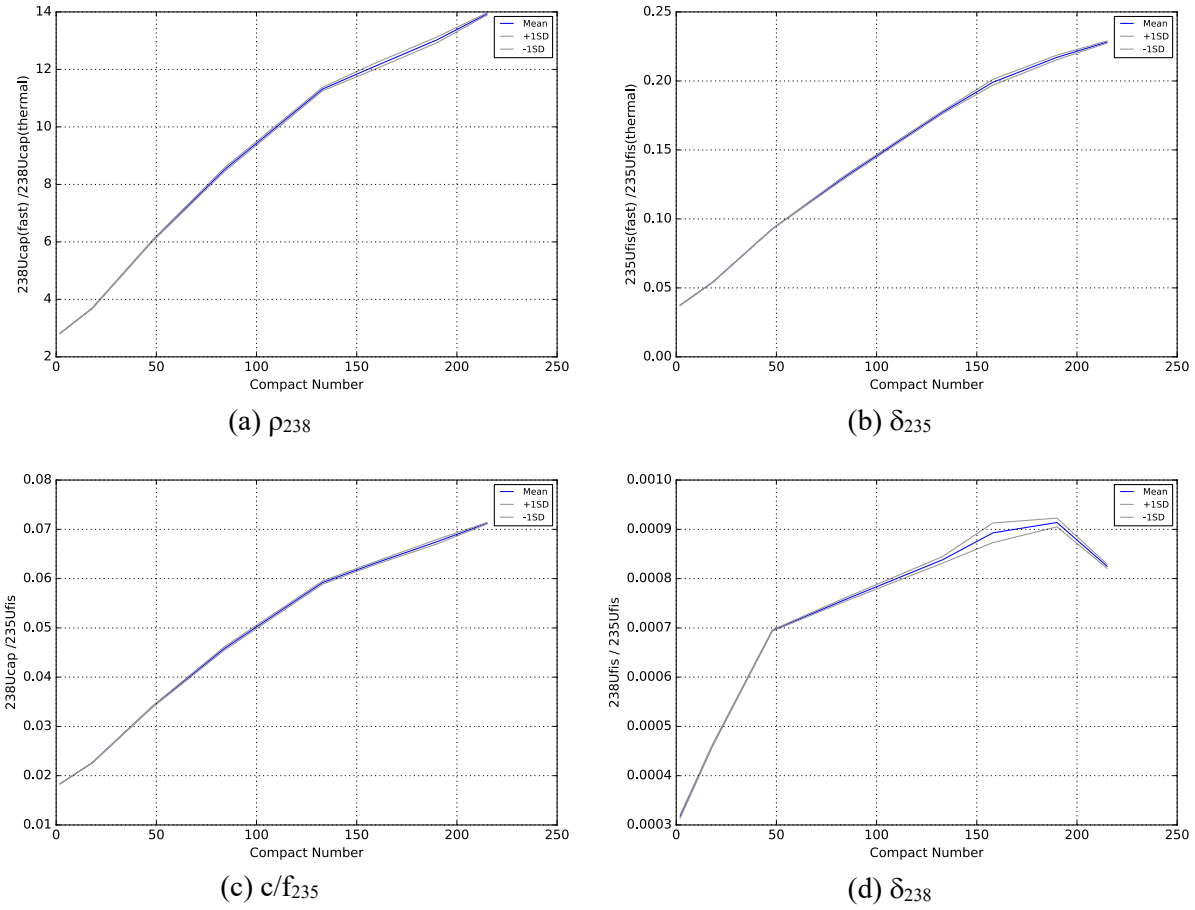

(a) ρ_{238} (b) δ_{235}

(c) c/f_{235} (d) δ_{238}

Source: OECD/NEA, 2020.

The hard spectrum is manifested in the values of ρ_{238} and δ_{235} (see Figure 8), which have now increased across the block leading to both an increase in ^{238}U capture and ^{235}U fast fission. The number of ^{238}U captures per fission event has increased more pronouncedly in the burned-fuel side. The ratio of ^{238}U to ^{235}U fissions appears to indicate an increase in the various spectral regions throughout the fuel block that manifests itself via the increase in the number of inflection points in this index.

Figure 6: Mean (a) value and RSD (b) of the peaking factors for case 1b

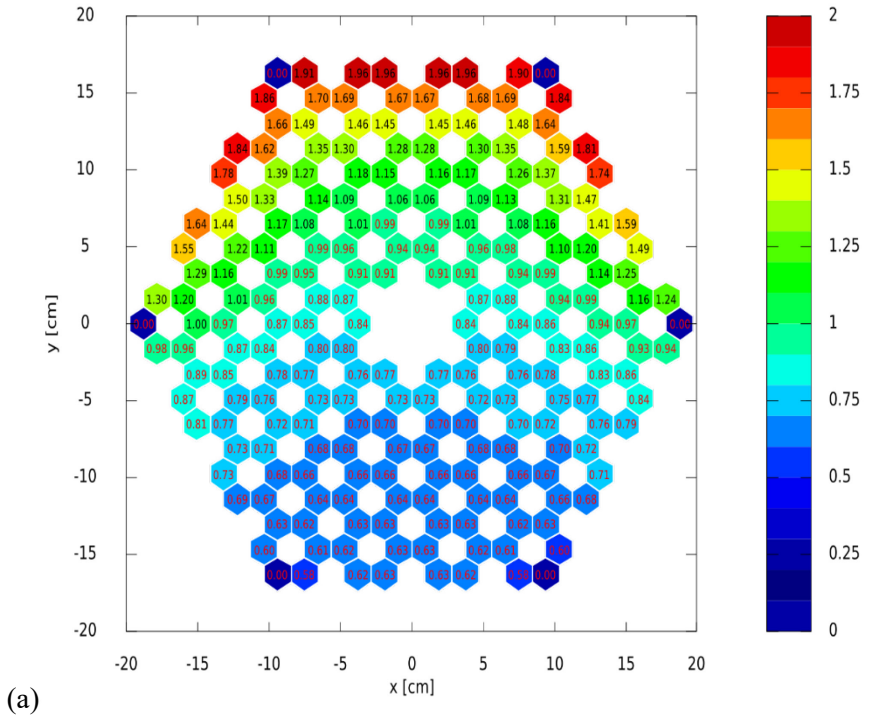

(a)

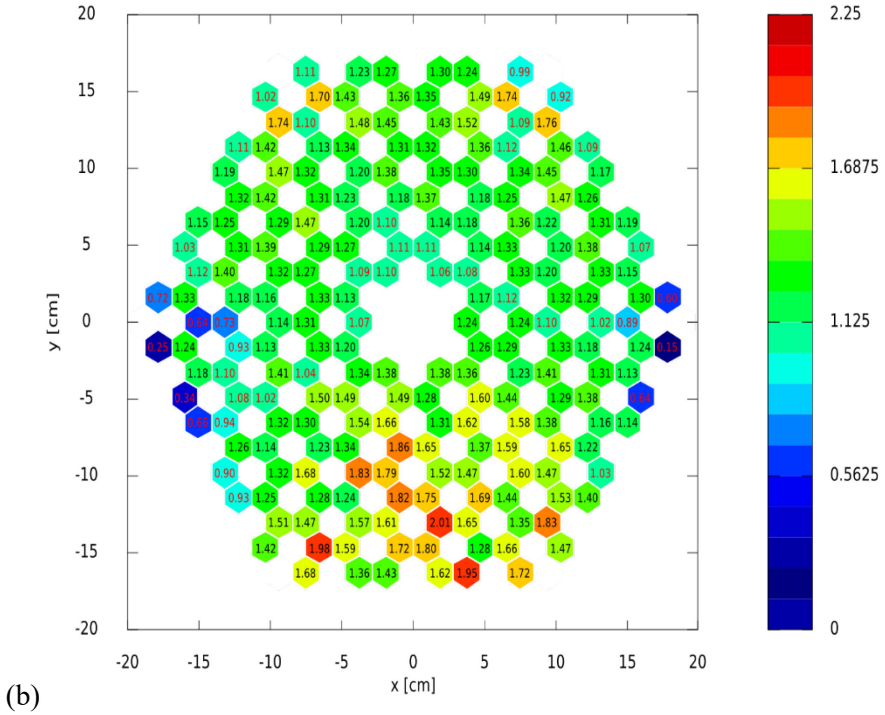

(b)

Source: OECD/NEA, 2020.

Figure 7: Neutron flux per lethargy for case 1b

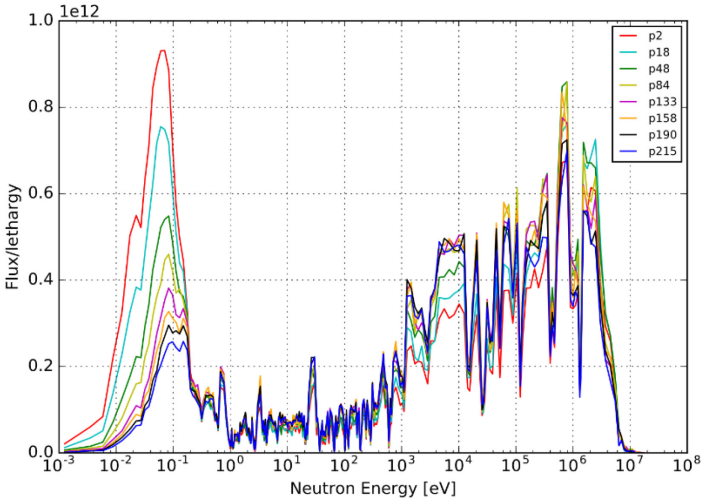

Source: OECD/NEA, 2020.

Figure 8: Spectral indices for case 1b

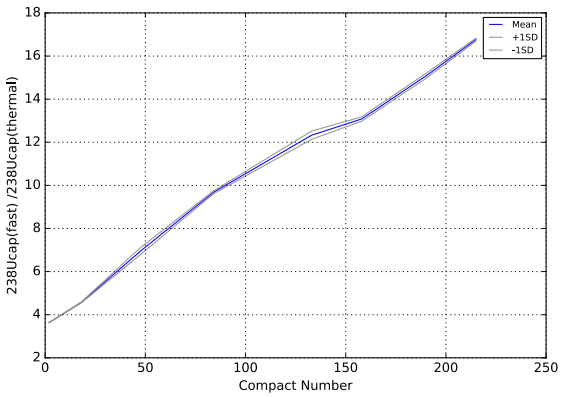

(a) ρ_{238}

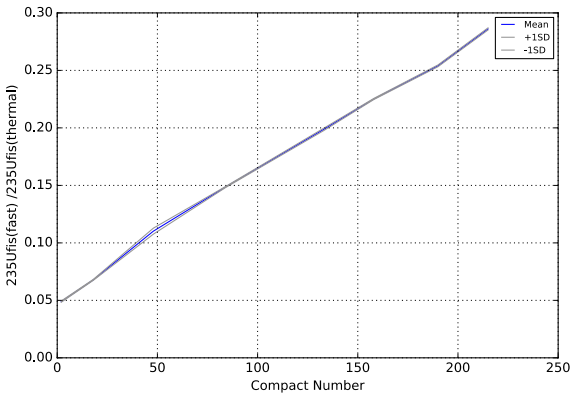

(b) δ_{235}

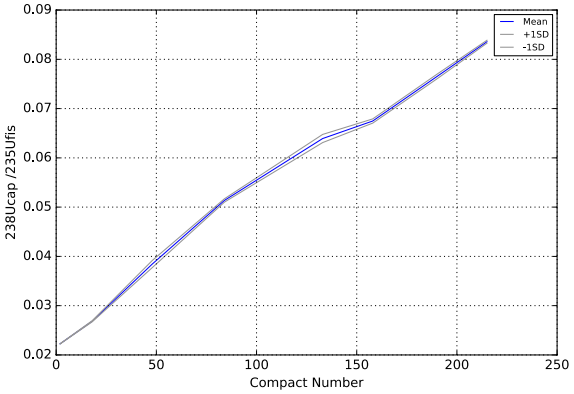

(c) c/f_{235}

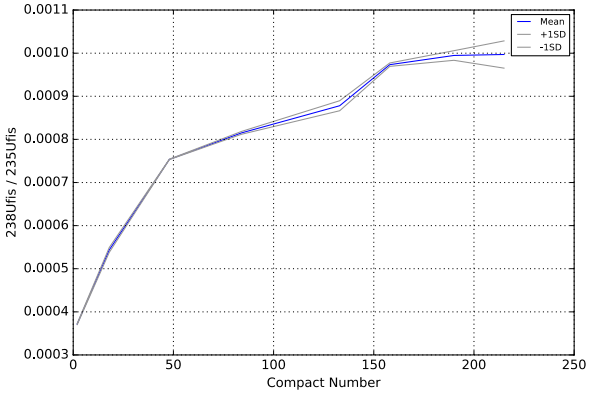

(d) δ_{238}

Source: OECD/NEA, 2020.

The reported cross-sections for the central block in Exercise 1 are shown in Table 5 and Table 6. There is good agreement in the thermal cross-sections (RSD <1%) for both cases 1a and 1b. The fast cross-sections show significant deviations in the Σ_t^1, Σ_a^1 and $\Sigma_{s,1\to1}$. The ~3% RSD in the Σ_t^1 is consistent with the values for both Σ_a^1 (3.2%) and $\Sigma_{s,1\to1}$ (2.9%). Further analysis of the data shows that the high deviation in the $\Sigma_{s,1\to1}$ is mainly attributed to DeCART, which is consistently 7% low in this exercise when compared to the Monte Carlo results, as shown in Table 7. The HELIOS result is low by 3% and 0.3% for case 1a and 1b when compared to the Monte Carlo results, but the inconsistency of the values is likely due to RPT methodology because the equivalent radius is calculated for fuel and for BP. More interesting is the low deviation in the $\nu\Sigma_f^1$ and Σ_f^1 results, which indicates that the large spread in the Σ_a^1 is very likely due to capture reactions or other neutron-disappearance reactions (n,x). Table 8 substantiates that; indeed, the deviation in the Σ_a^1 is primarily due to HELIOS and to potential issues in the RPT methodology with ^{238}U capture, which should dominate the absorption reaction excluding fission.

The presence of BPs has an obvious effect on the absorption cross-section, but, in addition, the harder spectrum effectively decreases thermal fission by 5% and increases fast fission by 1.7%. It also increases the down-scattering cross-section by 2.4%.

Table 5: Cross-sections for case 1a

	Mean [cm^{-1}]		Stdev. [cm^{-1}]		RSD [%]	
	g=1	g=2	g=1	g=2	g=1	g=2
Σ_t	2.854E-01	3.541E-01	8.222E-03	3.464E-03	2.88	0.98
Σ_a	1.262E-03	1.113E-02	4.033E-05	8.362E-05	3.20	0.75
$\nu\Sigma_f$	9.264E-04	2.213E-02	3.436E-06	1.654E-04	0.37	0.75
Σ_f	3.778E-04	9.080E-03	1.477E-06	6.771E-05	0.39	0.75
$\Sigma_{s,1\to g}$	2.821E-01	2.041E-03	8.187E-03	3.305E-05	2.90	1.62
$\Sigma_{s,2\to g}$ *	0	3.419E-01	0	3.320E-03	0	0.97

*does not include McCARD data

Source: OECD/NEA, 2020.

Table 6: Cross-sections for case 1b

	Mean [cm^{-1}]		Stdev. [cm^{-1}]		RSD [%]	
	g=1	g=2	g=1	g=2	g=1	g=2
Σ_t	2.883E-01	3.574E-01	8.516E-03	2.665E-03	2.95	0.75
Σ_a	1.399E-03	1.407E-02	3.654E-05	5.879E-05	2.61	0.42
$\nu\Sigma_f$	9.421E-04	2.108E-02	1.014E-06	1.539E-04	0.11	0.73
Σ_f	3.843E-04	8.652E-03	4.641E-07	6.316E-05	0.12	0.73
$\Sigma_{s,1\to g}$	2.848E-01	2.090E-03	8.525E-03	1.182E-05	2.99	0.57
$\Sigma_{s,2\to g}$ *	0	3.428E-01	0	2.970E-03	0	0.87

* does not include McCARD data

Source: OECD/NEA, 2020.

Table 7: Within group scattering cross-sections Exercise 1

	Case 1a		Case 1b	
	$\Sigma_{s,1\to1}$	$\Sigma_{s,2\to2}$	$\Sigma_{s,1\to1}$	$\Sigma_{s,2\to2}$
DeCART	2.694E-01	3.410E-01	2.701E-01	3.386E-01
HELIOS	2.805E-01	3.384E-01	2.891E-01	3.446E-01
McCARD	2.893E-01	-	2.900E-01	-
Serpent	2.893E-01	3.463E-01	2.902E-01	3.452E-01
mean	2.821E-01	3.419E-01	2.848E-01	3.428E-01
SD	8.187E-03	3.320E-03	8.525E-03	2.970E-03
RSD	2.9%	0.97%	2.99%	0.87%

Source: OECD/NEA, 2020.

Table 8: Absorption cross-sections Exercise 1

	no BPs		with BPs	
	g=1	g=2	g=1	g=2
DeCART	1.290E-03	1.114E-02	1.425E-03	1.409E-02
HELIOS	1.192E-03	1.099E-02	1.336E-03	1.397E-02
McCARD	1.282E-03	1.117E-02	1.417E-03	1.409E-02
Serpent	1.284E-03	1.121E-02	1.419E-03	1.413E-02
mean	1.262E-03	1.113E-02	1.399E-03	1.407E-02
SD	4.033E-05	8.361E-05	3.654E-05	5.878E-05
RSD	3.20%	0.75%	2.61%	0.42%

Source: OECD/NEA, 2020.

The four factors for case 1a and 1b are shown in Table 9 and Table 10, respectively. There is good agreement overall, with RSDs below 1.5%. When contrasting the cases with and without BP, we observe small effects on most parameters. The harder spectrum in case 1b increased the fast-fission factor roughly 1.9%, while decreasing the resonance escape by 1.1%. The value of eta mostly remains unchanged, which is consistent with the expected physics because the ratio of thermal-neutron production to thermal-neutron absorption in the fuel should remain constant. The factor that incurs the largest change is the thermal utilisation, which decreases by 25%. This drop is primarily due to the presence of BPs, which effectively increase the value of the thermal-absorption cross-section.

Table 9: Four factors for case 1a

	Mean	Stdev	RSD
Fast fission factor	1.116	1.330E-03	0.119
Resonance escape	0.996	1.904E-04	0.019
Thermal utilisation	0.974	1.396E-02	1.433
eta	2.043	2.774E-02	1.358

Source: OECD/NEA, 2020.

Table 10: Four factors for case 1b

	Mean	Stdev	RSD
Fast fission factor	1.137	1.138E-03	0.100
Resonance escape	0.995	2.282E-04	0.023
Thermal utilisation	0.735	7.873E-03	1.072
eta	2.041	2.825E-02	1.384

Source: OECD/NEA, 2020.

From the four factors, one can compute an infinite multiplication factor for each case, which yields the values of 1.79478 and 1.36196 for 1a and 1b, respectively.

Exercise 2 results

The multiplication factors from the depletion calculations in Exercise 2 are included in Table 11 and Table 12 with their respective reactivity curves plotted in Figure 9 and Figure 10. The results show good agreement among participants with standard deviations within 200 pcm during the entire depletion. Both Monte Carlo codes remain consistent within 100 pcm of one another, whereas the deterministic codes have a propensity for higher values. In both cases 2a and 2b DeCART shows a higher bias (~340 pcm), but with much lower standard deviation (~39 pcm). On the other hand, HELIOS has a lower overall bias (~160), but with larger standard deviation (~90 pcm). This appears to be an artefact of the RPT methodology and will be further examined with additional data. All participants consistently calculate the reactivity peak occurring near 50 GWd/MTU with BPs modelled.

Because power is constant throughout the depletion calculation, and the BP is designed to completely deplete within the life of the fuel block, the multiplication factors end at a similar point between cases 2a and 2b: 1.04647 versus 1.04561.

Table 11: Multiplication factors for case 2a

MWd/kg	HELIOS	DeCART	MCCARD	SERPENT	mean	SD
0.0	1.18103	1.18390	1.18119	1.18103	1.18180	123.9
0.5	1.17046	1.17120	1.16782	1.16693	1.16910	177.5
5	1.16345	1.16412	1.16123	1.15981	1.16215	172.4
10	1.15743	1.15824	1.15518	1.15392	1.15619	172.6
20	1.14504	1.14610	1.14273	1.14179	1.14392	172.9
30	1.13290	1.13408	1.13070	1.12975	1.13186	171.8
40	1.12120	1.12259	1.11925	1.11824	1.12032	168.8
50	1.10999	1.11170	1.10849	1.10746	1.10941	159.9
60	1.09935	1.10137	1.09780	1.09714	1.09892	162.9
70	1.08920	1.09156	1.08742	1.08728	1.08887	173.0
80	1.07949	1.08221	1.07839	1.07792	1.07950	166.4
90	1.07021	1.07330	1.06949	1.06893	1.07048	168.9
100	1.06135	1.06482	1.06089	1.06047	1.06188	172.4
120	1.04508	1.04963	1.04650	1.04467	1.04647	194.7

Source: OECD/NEA, 2020.

Figure 9: Multiplication factors for Exercise 2a

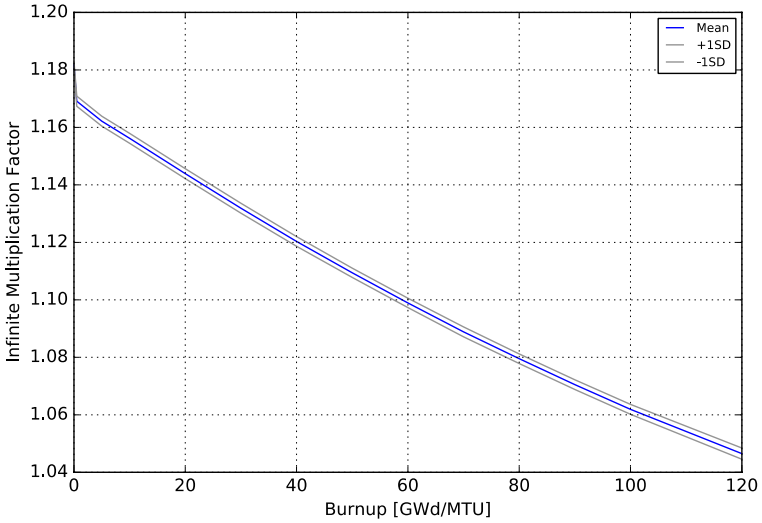

Source: OECD/NEA, 2020.

Table 12: Multiplication factors for case 2b

MWd/kg	HELIOS	DeCART	MCCARD	SERPENT	mean	SD
0.0	1.07681	1.07936	1.07624	1.07646	1.07722	125.4
0.5	1.06961	1.07133	1.06789	1.06793	1.06919	141.7
5	1.06950	1.07133	1.06801	1.06762	1.06912	145.9
10	1.07118	1.07304	1.06947	1.06920	1.07072	153.8
20	1.07650	1.07769	1.07396	1.07391	1.07552	163.5
30	1.08358	1.08398	1.08058	1.08049	1.08216	162.9
40	1.08866	1.08890	1.08674	1.08532	1.08741	146.6
50	1.08894	1.08959	1.08740	1.08565	1.08790	152.1
60	1.08561	1.08662	1.08397	1.08253	1.08468	156.2
70	1.08034	1.08159	1.07870	1.07744	1.07952	157.8
80	1.07374	1.07542	1.07237	1.07118	1.07318	158.0
90	1.06646	1.06870	1.06550	1.06436	1.06626	159.5
100	1.05900	1.06180	1.05836	1.05753	1.05917	160.4
120	1.04438	1.04859	1.04568	1.04380	1.04561	184.9

Source: OECD/NEA, 2020.

Figure 10: Multiplication factors for case 2b

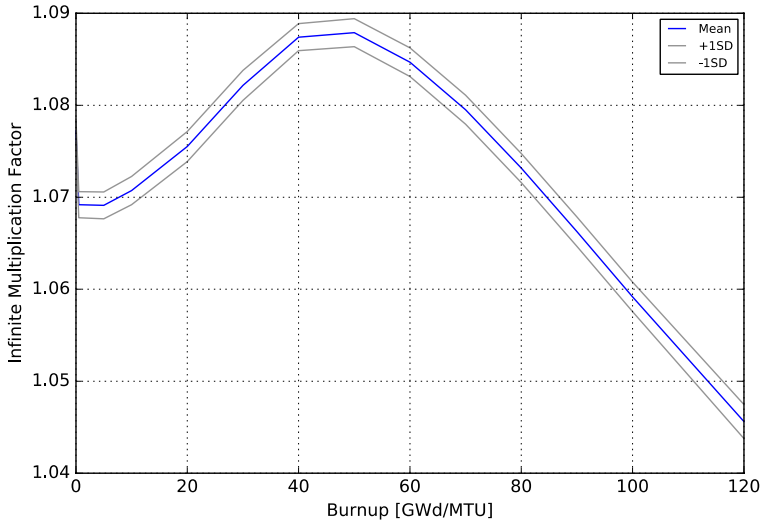

Source: OECD/NEA, 2020.

The change in the eigenvalue due to temperature at BOL is -4 385 and -5 553 pcm without and with BPs, respectively, when compared to Exercise 1 results. The BP reactivity worth as a function of burn-up for all participants, as well as the mean and standard deviation, are shown in Table 13. Even though the consistency of the standard deviation is very reasonable (<50 pcm), both deterministic codes show a bias in the results during the depletion, which can be due to the self-shielding methods.

Table 13: BP reactivity worth during depletion

MWd/kg	HELIOS	DeCART	MCCARD	SERPENT	mean	SD
0.0	-8.20%	-8.18%	-8.26%	-8.23%	-8.21%	28.0
0.5	-8.06%	-7.96%	-8.01%	-7.94%	-7.99%	44.2
5	-7.55%	-7.44%	-7.52%	-7.45%	-7.49%	47.0
10	-6.96%	-6.86%	-6.94%	-6.87%	-6.90%	43.8
20	-5.56%	-5.54%	-5.60%	-5.54%	-5.56%	27.1
30	-4.02%	-4.08%	-4.10%	-4.04%	-4.06%	33.1
40	-2.67%	-2.76%	-2.67%	-2.71%	-2.70%	36.0
50	-1.74%	-1.83%	-1.75%	-1.81%	-1.78%	37.4
60	-1.15%	-1.23%	-1.16%	-1.23%	-1.19%	37.5
70	-0.75%	-0.84%	-0.74%	-0.84%	-0.80%	47.2
80	-0.50%	-0.58%	-0.52%	-0.58%	-0.55%	38.6
90	-0.33%	-0.40%	-0.35%	-0.40%	-0.37%	31.9
100	-0.21%	-0.27%	-0.23%	-0.26%	-0.24%	24.5
120	-0.06%	-0.09%	-0.07%	-0.08%	-0.08%	10.9

Source: OECD/NEA, 2020.

Peaking factors for three depletion points (BOL, MOL and EOL) in both cases 2a and 2b are presented in Figures 11-16. The RSDs at BOL are both similar in distribution and magnitude to those encountered in case 1a and 1b, which means that these calculations are consistent with those at low temperature. A significant reduction in the maximum peaking factors is obtained from the temperature effects: ~14% at BOL for both cases. The higher temperature tends to redistribute the power and reduce the power gradient across the block (Figure 11). This tendency is further promoted by the presence of the BPs in Figure 12, leading to the flattest power distribution at BOL.

As the fuel depletes to MOL, the peaking factors flatten further as the higher power relocates to the least-burned fuel regions. The presence of the BPs in Figure 14 leads to a larger gradient and higher peaking at this point. The agreement among participants is quite good at MOL, with RSDs below 1.74%.

At EOL, the distribution of peaking factors is very similar between case 2a and 2b because the effects of the BP have subsided. The RSDs between participants show consistency for both cases, with maximum values below 2.5%.

The presence and evolution of this power gradient leads to differences in the depletion of fuel because the thermal side of the block experiences higher average powers and, therefore, considerably more depletion of ^{235}U. One can observe a similar power distribution at EOL between cases 2a and 2b because the power is fixed and the BP is designed to burn out. Interestingly, results from the ^{10}B concentrations, which are presented later, show that the BP is only depleted in the thermal zone of the reflectors. In addition, there might be an inherent benefit to loading all six vertices of the fuel block with BPs, due to increased ^{239}Pu production to further extend the life of the fuel.

Figure 11: Mean (a) value and RSD (b) of the peaking factors for case 2a at BOL

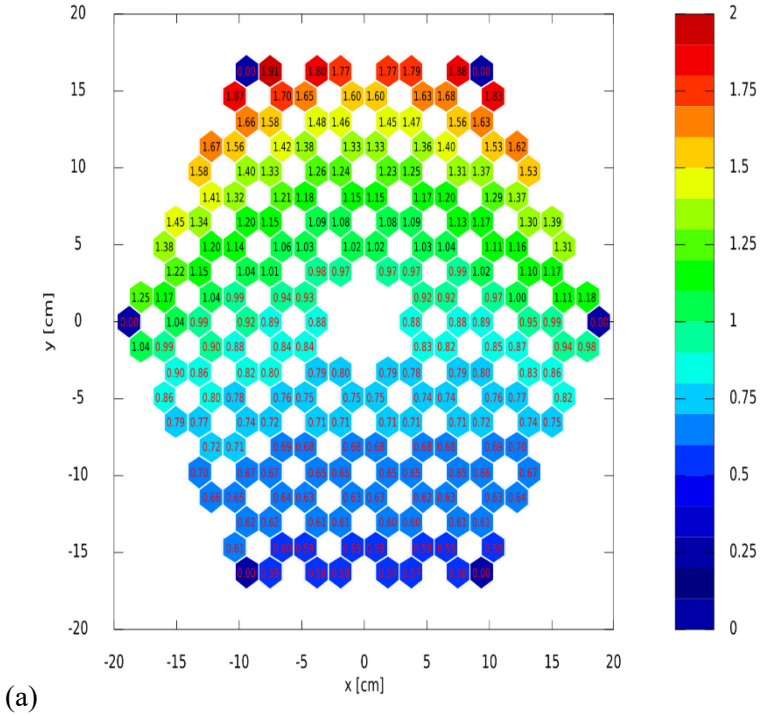

(a)

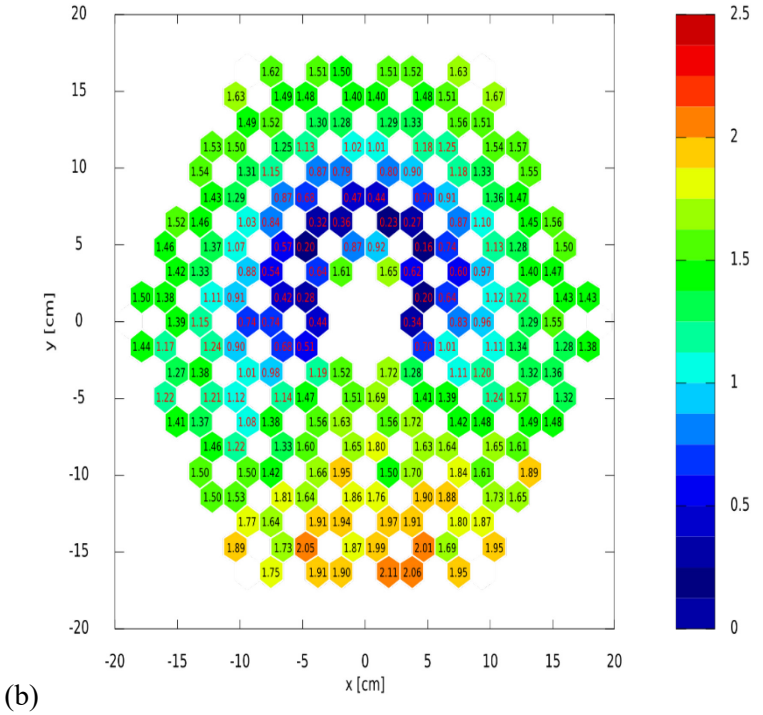

(b)

Source: OECD/NEA, 2020.

Figure 12: Mean (a) value and RSD (b) of the peaking factors for case 2b at BOL

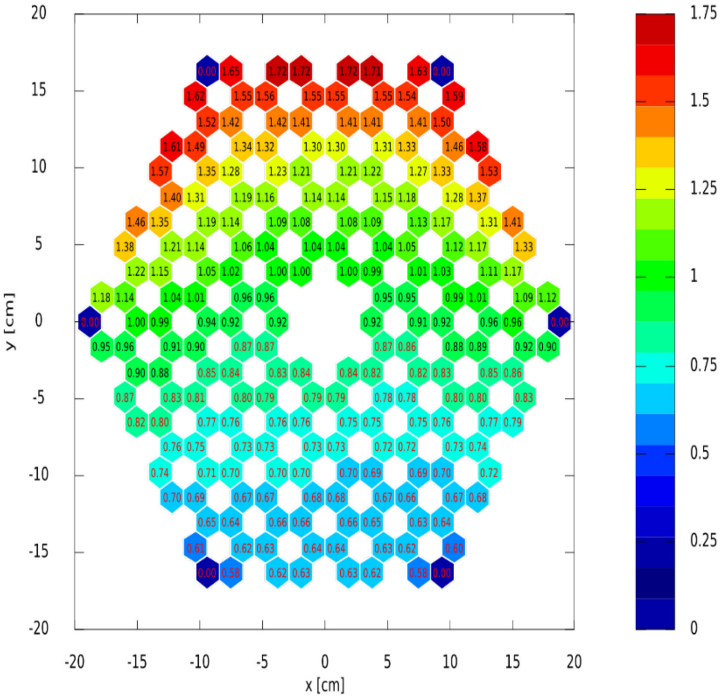

(a)

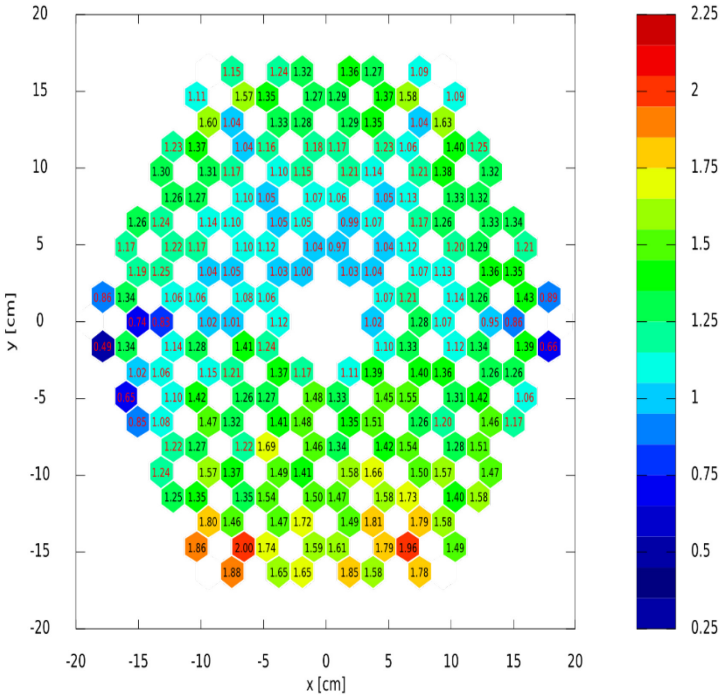

(b)

Source: OECD/NEA, 2020.

Figure 13: Mean value and RSD of the peaking factors for case 2a at 60 MOL

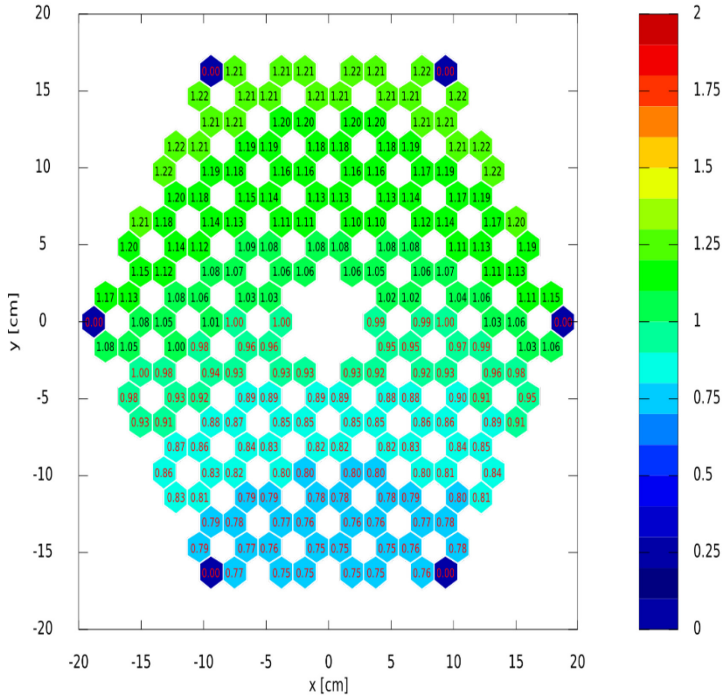

(a)

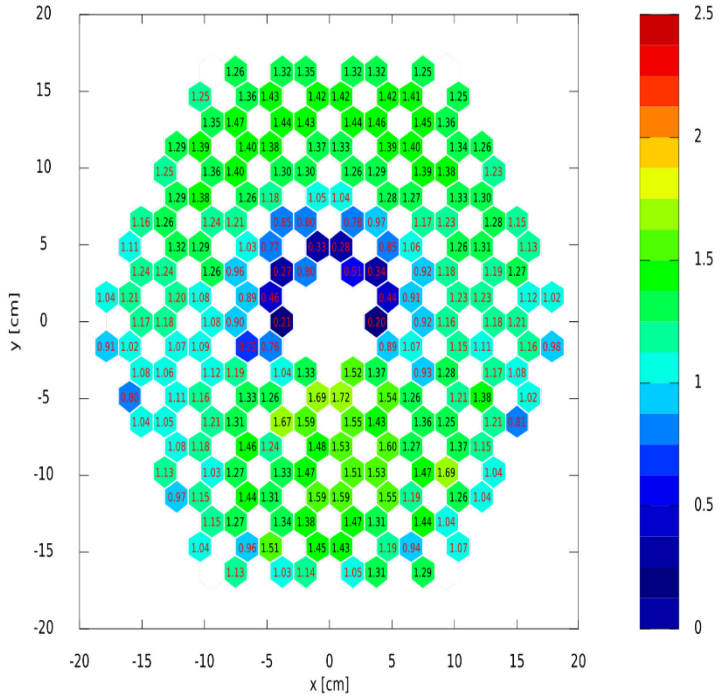

(b)

Source: OECD/NEA, 2020.

Figure 14: Mean (a) value and RSD (b) of the peaking factors for case 2b at 60 MOL

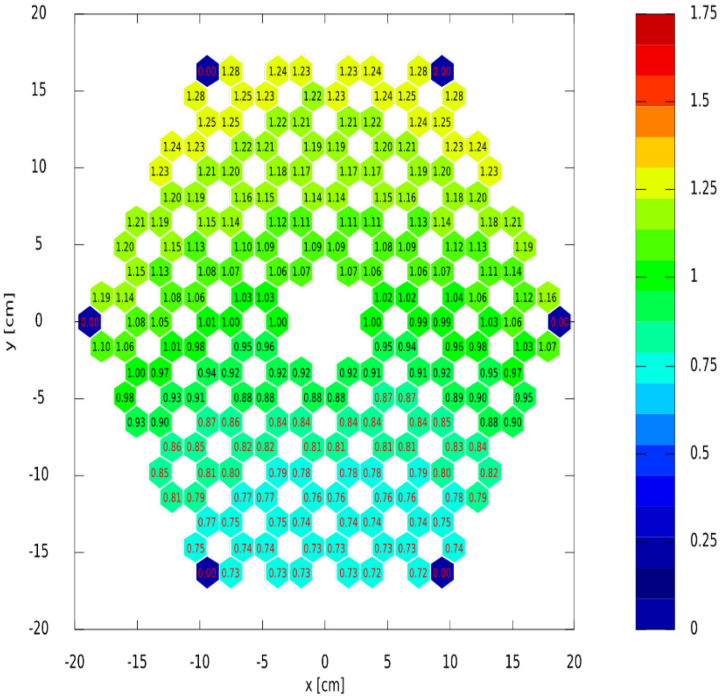

(a)

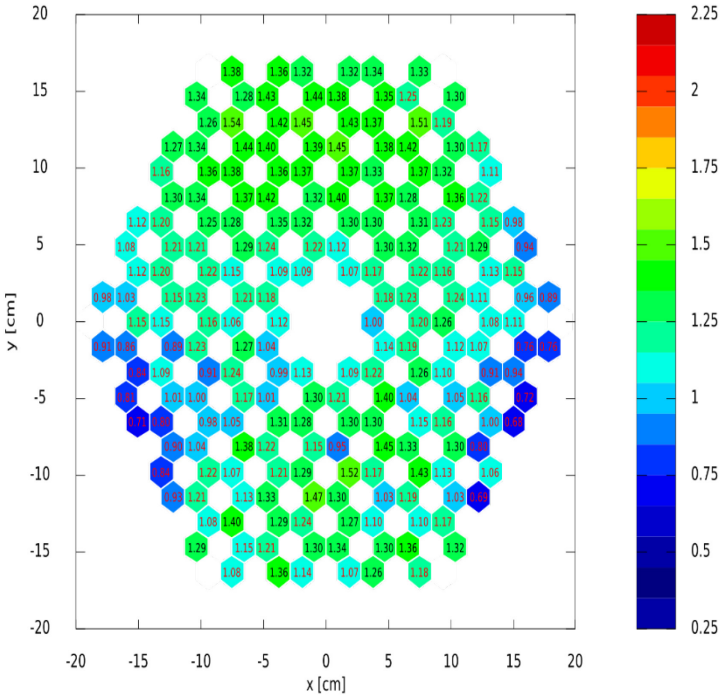

(b)

Source: OECD/NEA, 2020.

Figure 15: Mean value and RSD of the peaking factors for case 2a at EOL

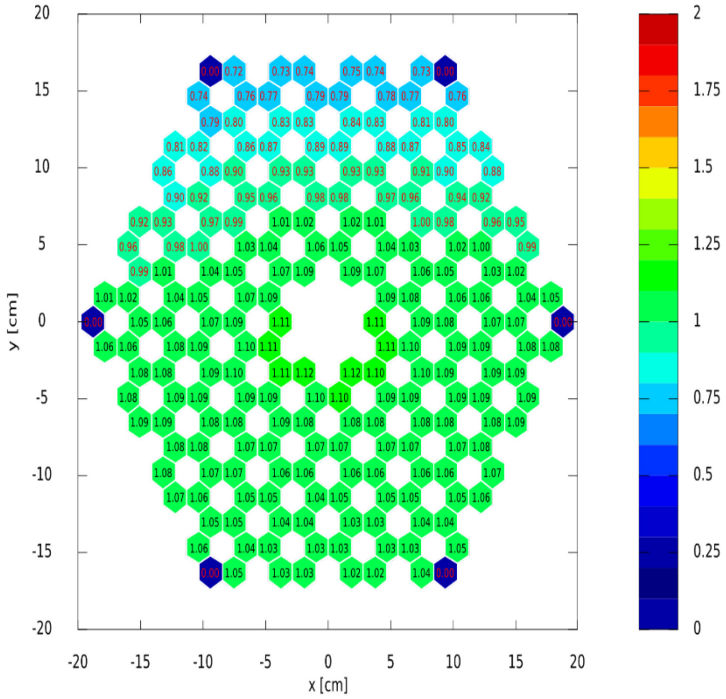

(a)

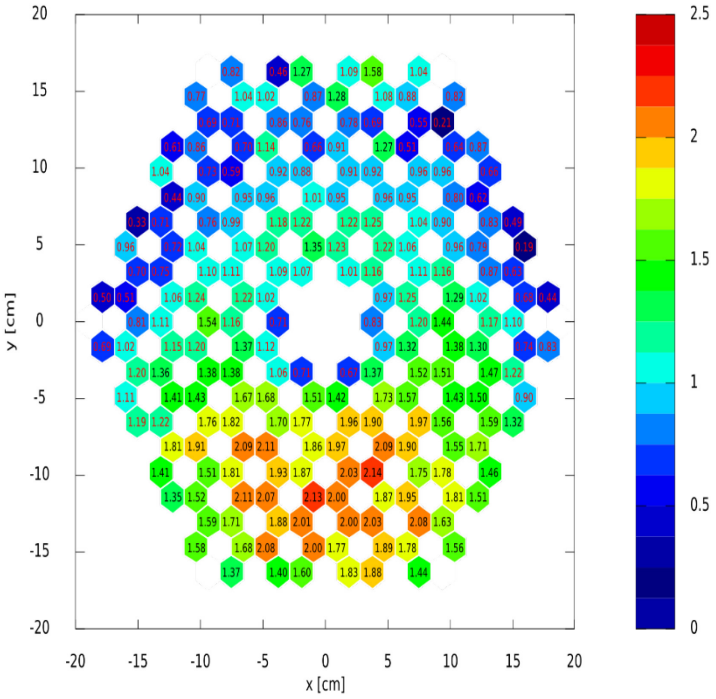

(b)

Source: OECD/NEA, 2020.

Figure 16: Mean value and RSD of the peaking factors for case 2b at EOL

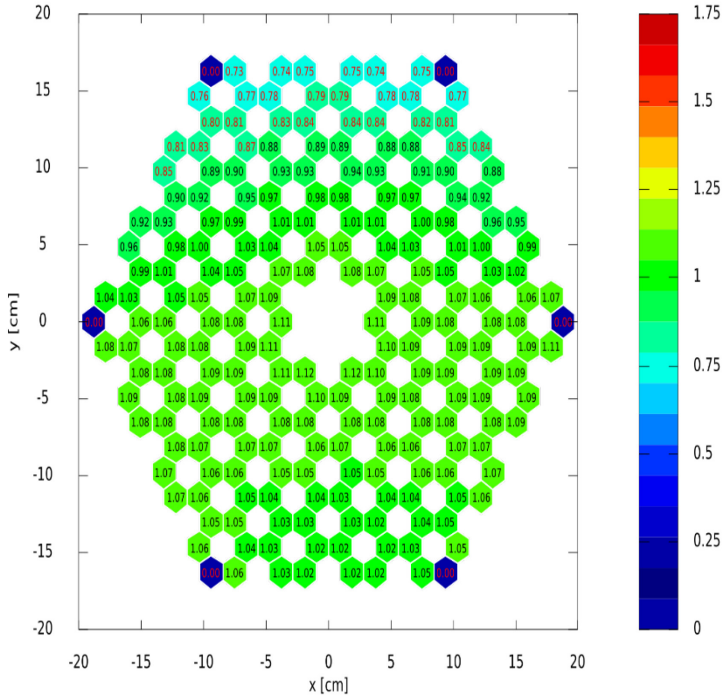

(a)

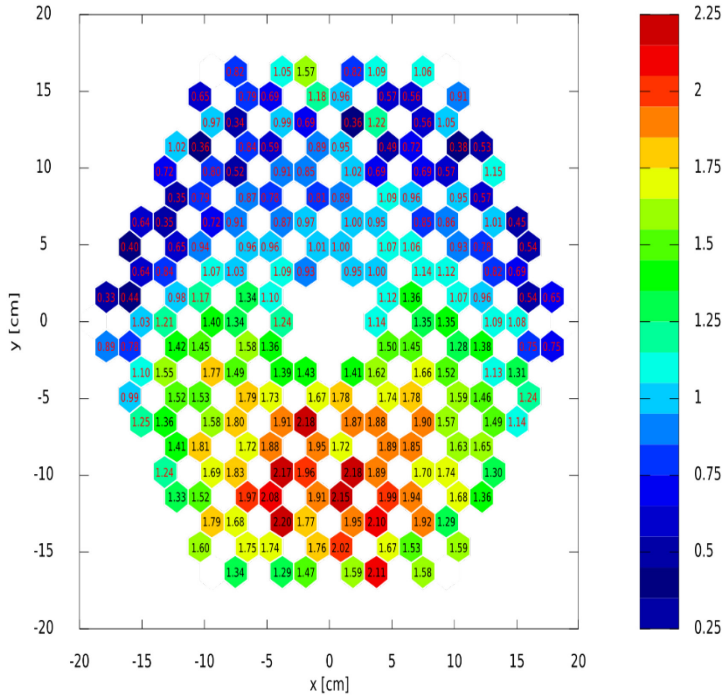

(b)

Source: OECD/NEA, 2020.

The distinct neutron-spectral zones of the central fuel block that were observed in cases 1a and 1b progress differently through the depletion. In all cases, the spectrum softens with depletion. Plots of flux per unit lethargy from Serpent in various compact positions across the block are included in Figure 17 and Figure 18. There are some significant differences where the large change in the thermal peak occurs between BOL and EOL in the thermal side of the block (Figure 17 [a] and [b]), whereas in the burned-fuel side (Figure 18 [a] and [b]) thermal peak is delayed and occurs between MOL and EOL. The change in the thermal peak in both regions is roughly 20% for the BP case and smaller in magnitude for the case without BPs.

Figure 17: Neutron energy spectra in compact 2 as a function of burn-up

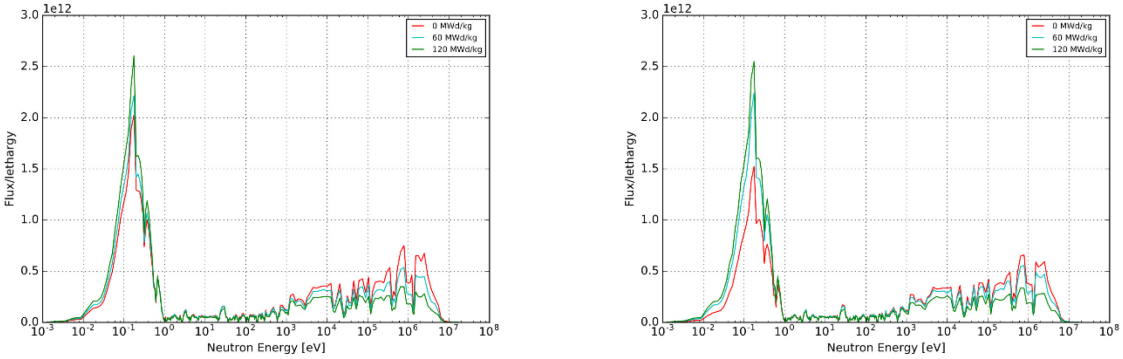

(a) no BP (b) with BP

Source: OECD/NEA, 2020.

Figure 18: Neutron energy spectra in compact 215 as a function of burn-up

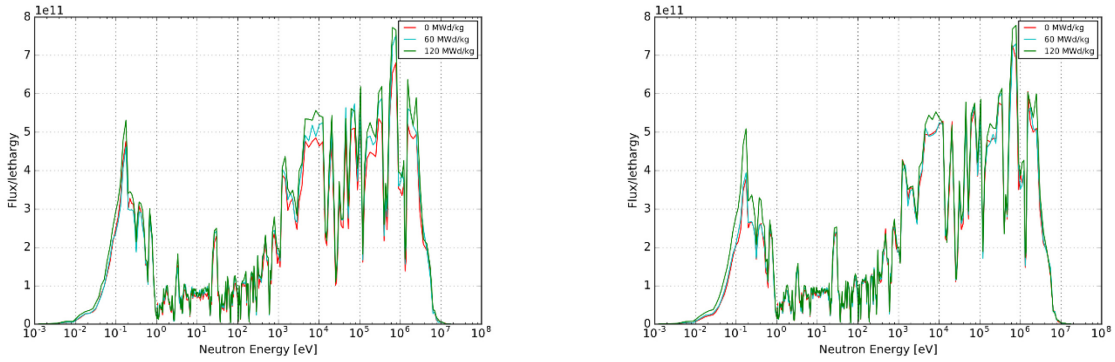

(a) no BP (b) with BP

Source: OECD/NEA, 2020.

The implications of this neutron-energy-spectrum distribution can be further examined through the spectral indices, which are based on results from both MC codes. The effects of the BPs on the ratio of ^{235}U fast to thermal fission (δ_{235}) in the thermal side of the block are shown in Figure 19. The BOL values are 20–26% higher near the reflector zone as compared to the low-temperature cases, whereas a consistent 12% increase is observed near the burned-fuel zone. This indicates that there is larger variability in the thermal region due to temperature. The effect of BPs has now been slightly diminished, from 30% to 23% when compared to the low-temperature cases. As the fuel burns near the reflector, δ_{235}

remains fairly linear, with a small dip in the presence of BPs. Conversely, the spectral effects are more dramatic near the burned-fuel region (see Figure 20), where the values of δ_{235} are 81% higher, thus promoting more fast fissions in ^{235}U. The time evolution of this spectral index is parabolic in nature without BPs, which indicates a propensity for fast ^{235}U fission between 20–80 GWd/MTU. The presence of BPs creates a significantly more linear behaviour, with the exception of an initial increase, but it is worth mentioning that there is a much larger change in its magnitude.

Figure 19: δ_{235} in compact 2

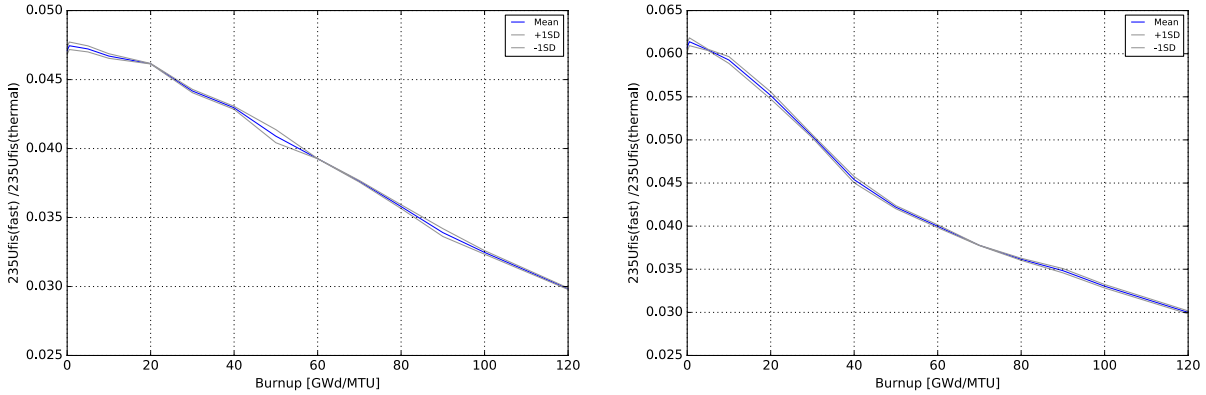

(a) no BP (b) with BP

Source: OECD/NEA, 2020.

Figure 20: δ_{235} in compact 215

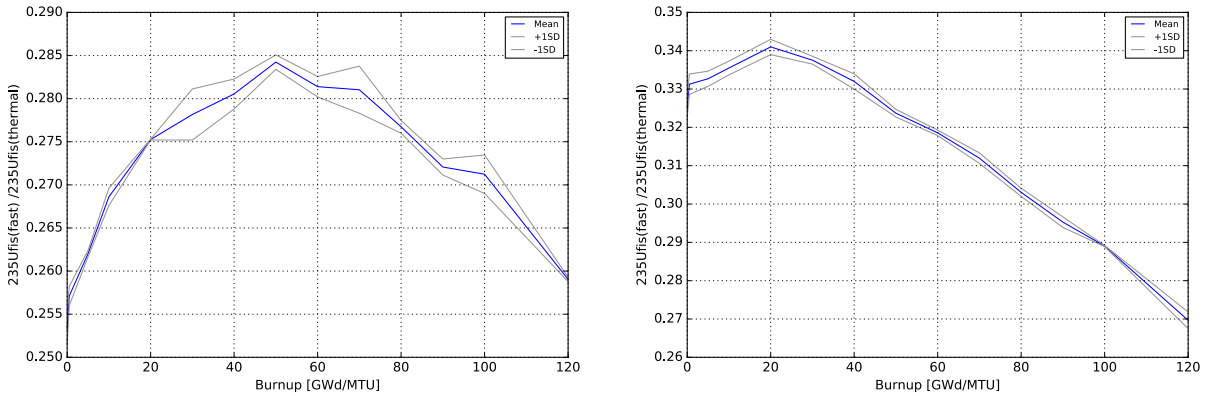

(a) no BP (b) with BP

Source: OECD/NEA, 2020.

The same basic pattern is repeated in the rest of the spectral indices included in Figures 21-26 due to spectral dependence. The presence of BPs increases the initial ratio of ^{238}U to ^{235}U fissions (δ_{238}) by 16% in both spatial regions of the fuel block. The hard-spectrum region of the block produces 2.6 times more ^{238}U fissions at BOL, with a milder variation in absolute value during depletion when compared to the thermal-spectrum zone.

Figure 21: δ_{238} in compact 2

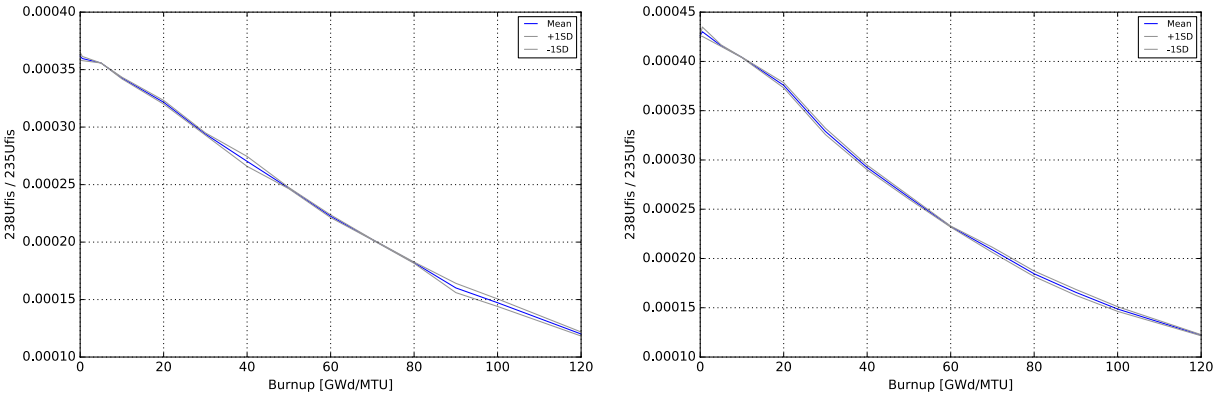

(a) no BP (b) with BP

Source: OECD/NEA, 2020.

Figure 22: δ_{238} in compact 215

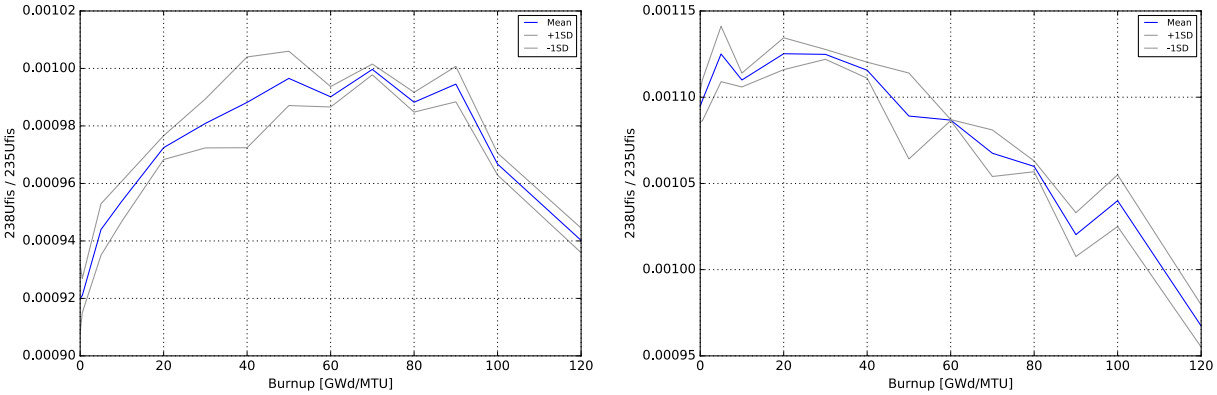

(a) no BP (b) with BP

Source: OECD/NEA, 2020.

The fast-to-thermal capture in ^{238}U (ρ_{238}) indicates a value that is 4.5 higher in the compact with the hardest spectrum. Therefore, this region should exhibit a much larger higher actinide production during the fuel depletion. This is also corroborated by the factor of 4 increase in the ^{238}U capture per ^{235}U fission (c/f_{235}) in the hard-spectrum zone. This effectively leads to large discrepancy in the production of actinides in both regions of the block.

Figure 23: ρ_{238} in compact 2

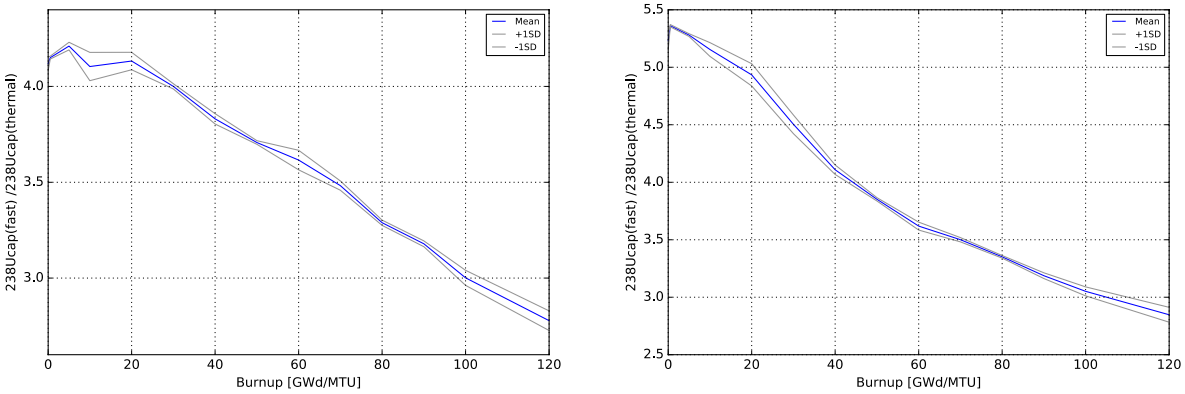

(a) no BP (b) with BP

Source: OECD/NEA, 2020.

Figure 24: ρ_{238} in compact 215

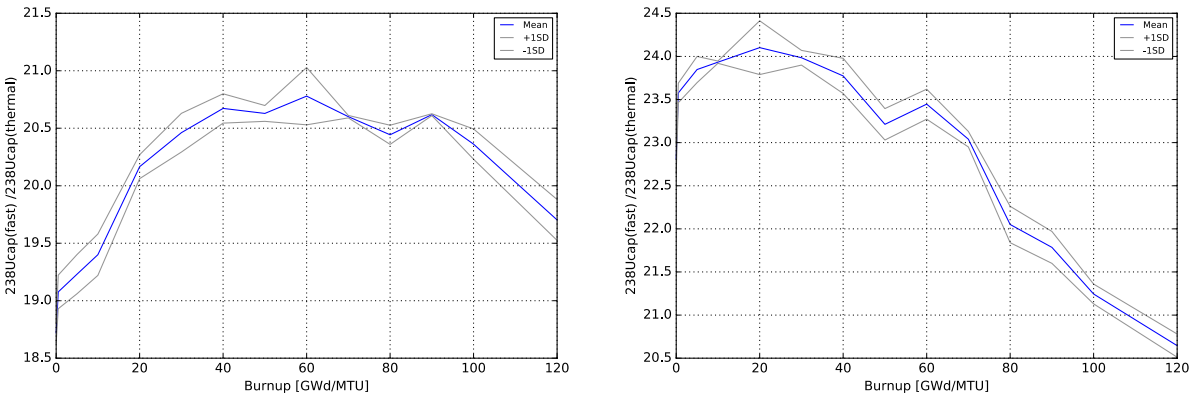

(a) no BP (b) with BP

Source: OECD/NEA, 2020.

Figure 25: c/f_{235} in compact 2

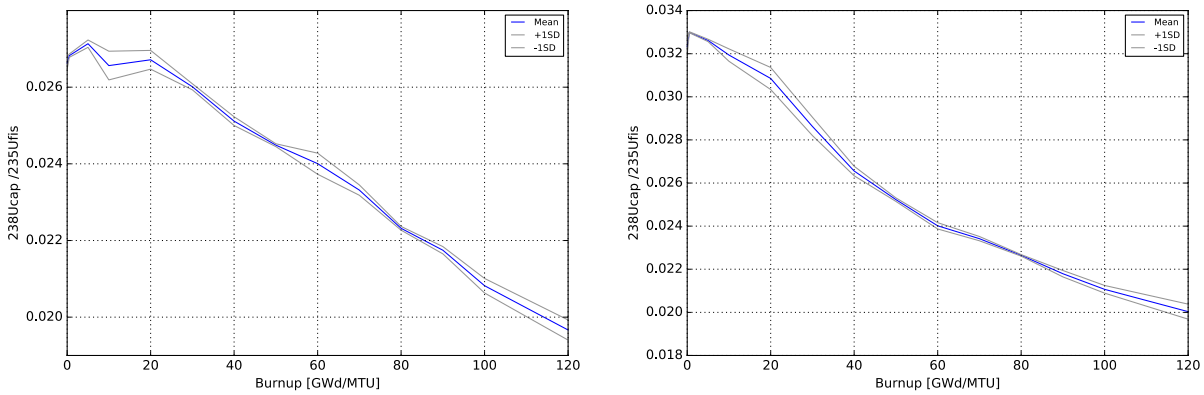

(a) no BP (b) with BP

Source: OECD/NEA, 2020.

Figure 26: c/f_{235} in compact 215

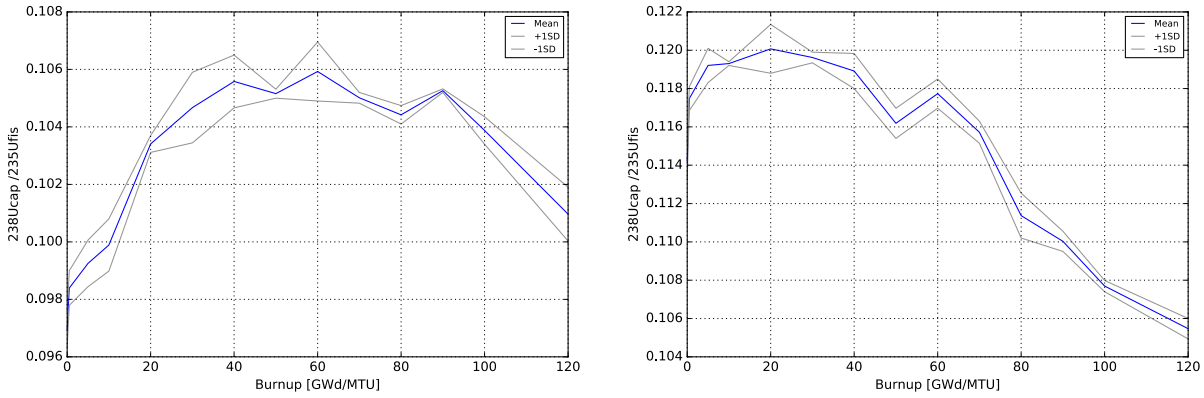

(a) no BP (b) with BP

Source: OECD/NEA, 2020.

The fast- and thermal-fission cross-sections calculated by each participant for Exercise 2 are shown in Figure 27 and Figure 28, respectively. The results show that there is very good consistency between the MC and the values obtained with the subgroup method. In contrast, there appears an emerging discrepancy in the RPT methodology used with HELIOS in both the thermal and fast range. The presence of BPs has a small effect on the fission cross-section across the block because the change in the shape of the energy spectrum in the low-energy range has little effect.

Figure 27: Fast-fission cross-sections for Exercise 2

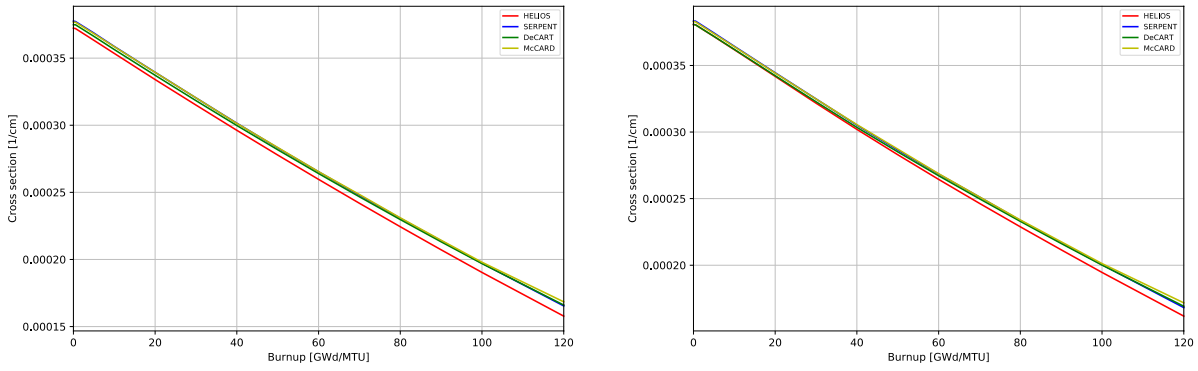

(a) no BP (b) with BP

Source: OECD/NEA, 2020.

Figure 28: Thermal-fission cross-sections for Exercise 2

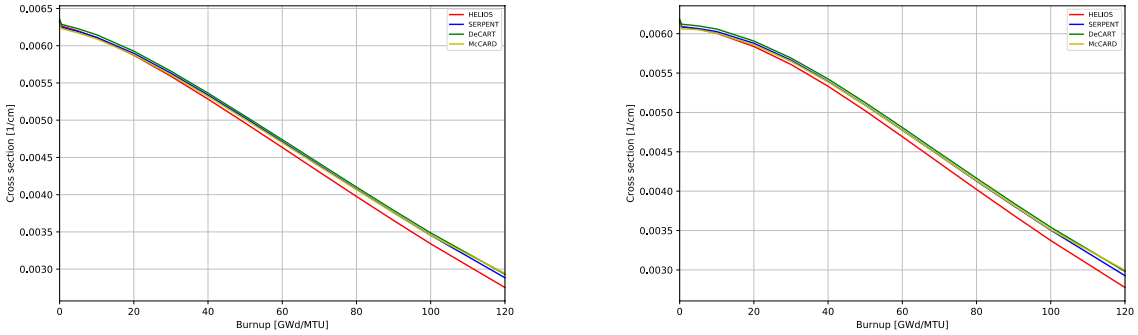

(a) no BP (b) with BP

Source: OECD/NEA, 2020.

The small differences observed in the fission cross-section with the RPT method are intensified in the fast and thermal-absorption cross-sections in Figure 29 and Figure 30. The RPT, which aims to preserve the integral reactivity of the fuel, cannot preserve the neutron energy self-shielding effect, thus leading to ~7% drop in the fast-absorption cross-section. Fast absorption is dominated by ^{238}U neutron radiative capture, which leads directly to the production of higher actinides. Thus, one expects to see discrepancies in actinide generation due to the self-shielding method. The effects on thermal absorption are less marked because the cross-section is governed by both ^{235}U and ^{239}Pu fission, but they do become apparent as the ^{239}Pu inventory builds up.

Figure 29: Fast-absorption cross-sections for Exercise 2

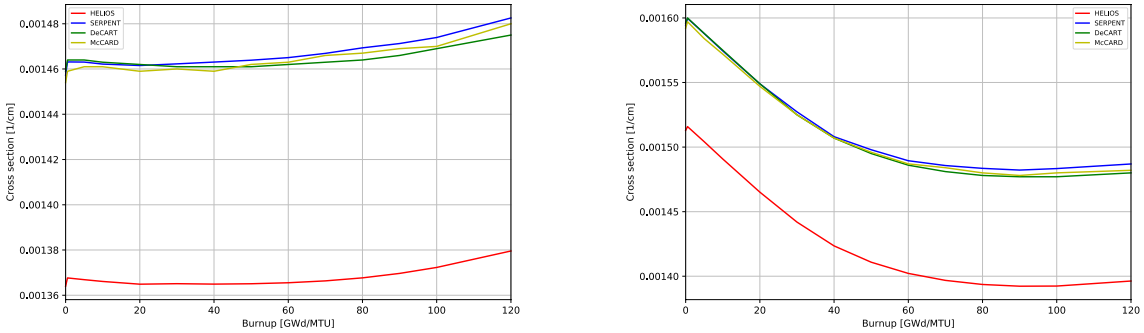

(a) no BP (b) with BP

Source: OECD/NEA, 2020.

Figure 30: Thermal-absorption cross-sections for Exercise 2

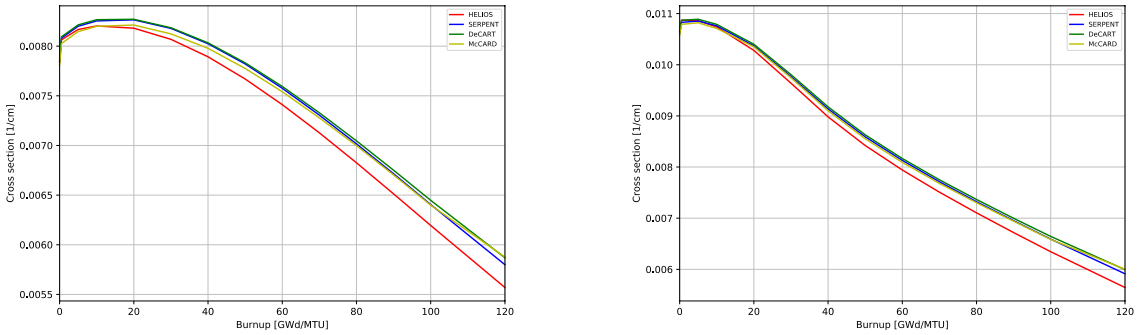

(a) no BP (b) with BP

Source: OECD/NEA, 2020.

Figure 31: ^{10}B relative concentrations

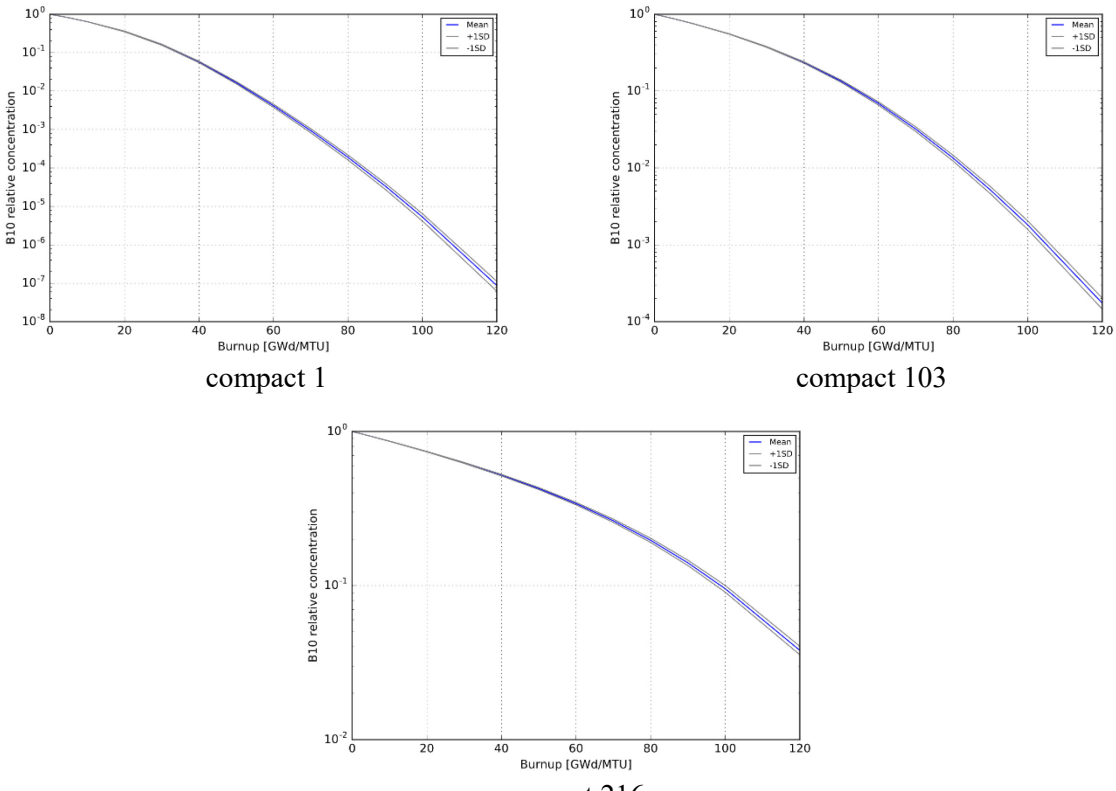

compact 1 compact 103

compact 216

Source: OECD/NEA, 2020.

Figure 31 shows the variation in depletion of ^{10}B at the reporting locations: (a) next to the reflector; (b) mid-block; and (c) near the burned fuel. Overall, there is good agreement between the various participants in each location, and the results indicate that RPT methodology performs quite well for ^{10}B depletion in this problem. It is interesting to note the large difference in the relative concentrations of ^{10}B in the various regions. There are three orders of magnitude difference between the thermal-spectrum region and the mid-

block, and an additional two orders of magnitude exist between the latter and the hard-spectrum region. Therefore, across the block, one observes five orders of magnitude difference. This is entirely driven by the difference in the spectrum and the shift in flux distribution during depletion.

The depletion and build-up of actinides are similar between both cases 2a and 2b, changing only in magnitude. Therefore, only the results in the presence of BPs are included in this report. Furthermore, two compact locations that represent the two spectral zones are selected to present the results and provide a good contrast to better understand depletion effects on a reactor-like configuration.

The depletions of ^{235}U and ^{238}U are shown in Figure 32. There is good agreement among participants for ^{235}U, but for ^{238}U, the uncertainty increases significantly during the depletion in both spectral zones. This is mainly due to the RPT method, and this is evident in Figure A.1. The ^{235}U concentration at EOL is ~6–7 times smaller in the soft-spectrum zone than in the hard one while the ^{238}U depletion differs only by 10%. The ^{235}U concentration in the thermal-spectrum zone is close to reaching its minimum value whereas, in the hard-spectrum zone, it is only halfway through its depletion. This implies that the higher actinides make a significant contribution to power generated in the thermal zone, as shown in Figure 16. This is observed in the production of ^{239}Pu and ^{241}Pu in Figure 33 and Figure 34, which confirm that ^{239}Pu reaches its maximum point at 30 GWd/MTU, while ^{241}Pu reaches saturation near 90 GWd/MTU.

Figure 32: ^{235}U and ^{238}U concentrations

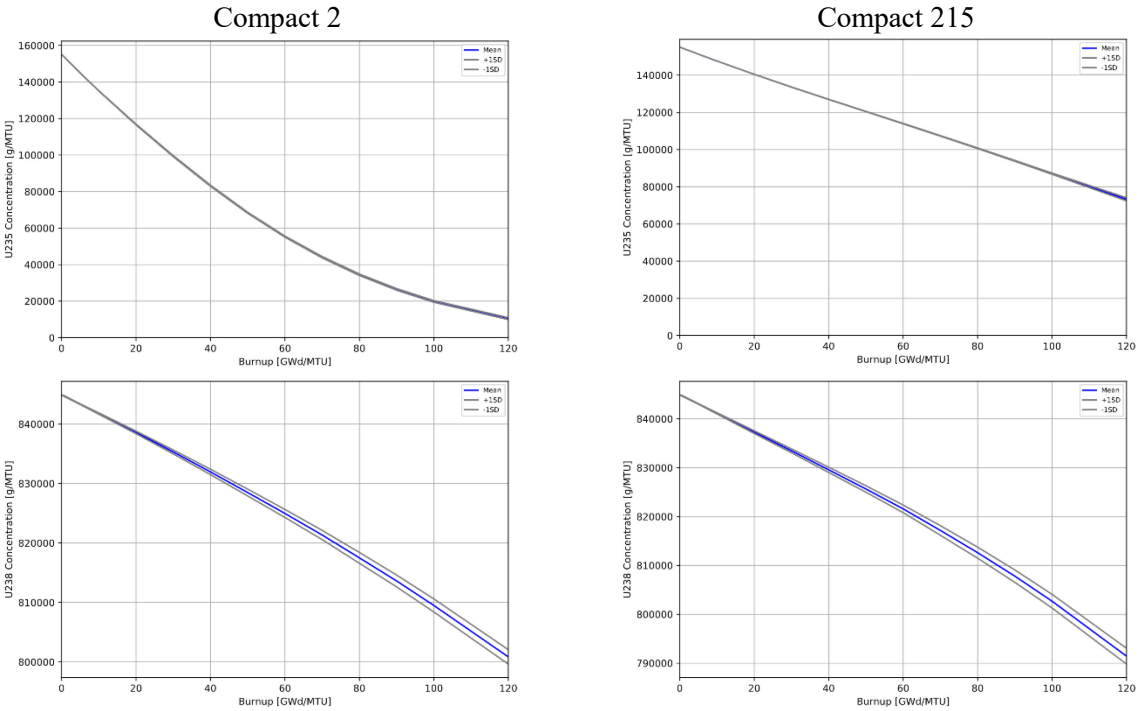

Source: OECD/NEA, 2020.

In the hard-spectrum zone, ^{239}Pu saturates near EOL while ^{241}Pu does not level off. The peak production of ^{239}Pu is four times higher near the burned fuel due to the higher capture rate in ^{238}U. More details of the spatial distribution of ^{239}Pu are provided in Figure A.2, which reveals that the ^{239}Pu concentration is decreasing in compact 133 (past the midpoint of the block) at 80 GWd/MTU. The participant's results for the Pu isotopes can be found in Figure A.2 through Figure A.5.

Figure 33: ^{239}Pu and ^{240}Pu concentrations

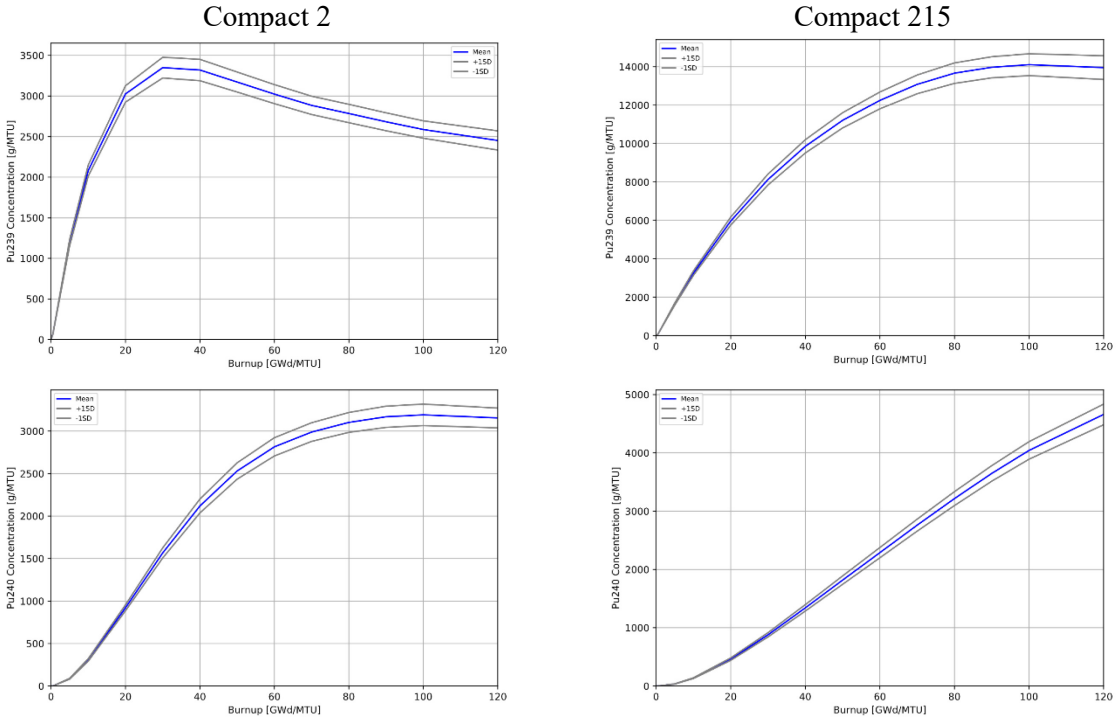

Source: OECD/NEA, 2020.

The mean concentrations for ^{244}Cm and ^{245}Cm are included in Figure 35, with a larger deviation in ^{245}Cm due to both DeCART and HELIOS, but showing a spectral dependence. These plots are supplemented with the participants' results in Annex A, Figure A.6. The discrepancies in the ^{245}Cm production could result from poor predictions of ^{241}Am. Coincidentally, there exists a large deviation in the mean concentrations of ^{241}Am, which are driven by the RPT method and the Serpent results. The deviation is included in Figure 36. The ^{241}Am concentration depends primarily on time-dependent concentration of ^{241}Pu through a double neutron capture of ^{239}Pu:

$$^{239}_{94}Pu \xrightarrow{(n,y)} {}^{240}_{94}Pu \xrightarrow{(n,y)} {}^{241}_{94}Pu \xrightarrow{\beta^-} {}^{241}_{95}Am.$$

Figure 34: ^{241}Pu and ^{242}Pu concentrations

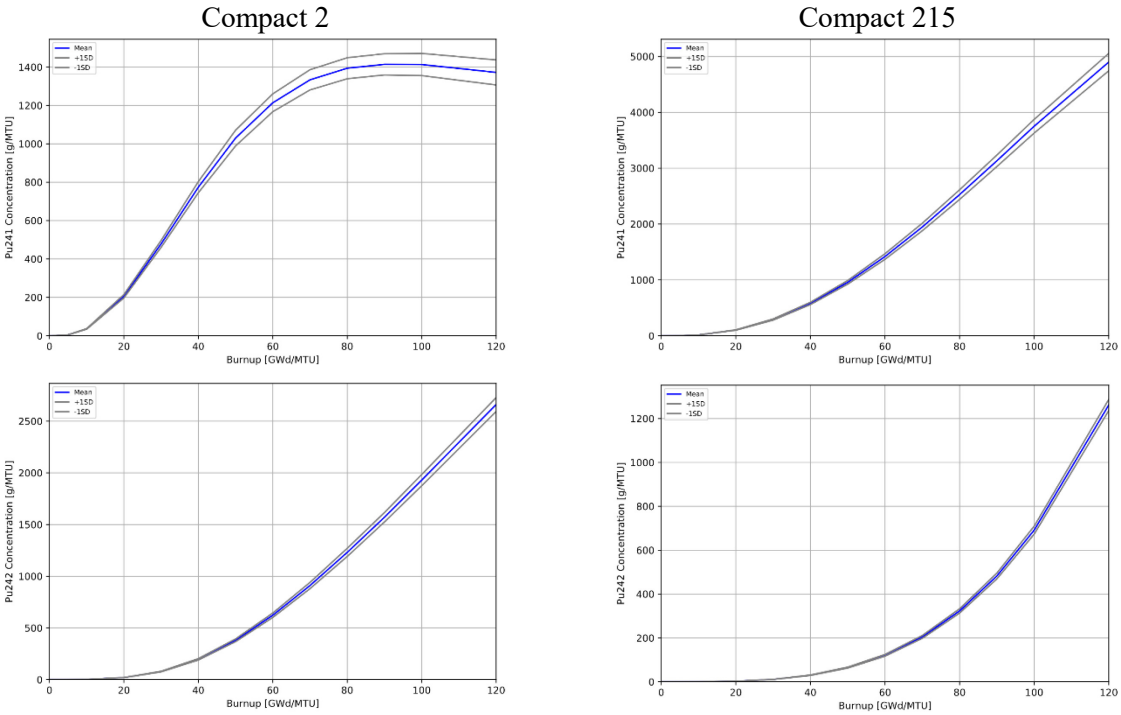

Source: OECD/NEA, 2020.

Because the RPT method with HELIOS under predicts the concentration of the Pu isotopes (see Annex A), it follows that it will under predict the concentration of ^{241}Am. On the other hand, the production of Pu isotopes by Serpent is quite consistent with the other codes, which implies that the problem might be in the ^{241}Pu decay or branching values to ^{242}Am and ^{242m}Am. Additional results for ^{241}Am concentrations are shown in Figure A.7.

The concentration of selected fission products is discussed next. Again, no significant effects on the time evolution of the fission-product concentrations are seen, without and with BPs, and only the magnitude of the local concentration is affected. The mean concentrations of ^{135}Xe and ^{85}Kr are included in Figure 37. The ^{135}Xe concentrations by the various participants are very consistent in both spectral zones of the central reflector. The Serpent results show a significant disagreement in the ^{85}Kr concentration, but this isotope is often troublesome, and various codes use different decay constants. In this case, the decay constants were confirmed to be very close and consistent with the ENDF/B-VII.r0 value of 2.04207E-09 s^{-1}. Thus, another possible explanation for the complex production of ^{85}Kr though fission in both ground and metastable states. The cumulative fission yield of ^{85m}Kr is higher, and the isotope has branching fractions of 79% β^- and 21% isomeric transition. Additional information will be needed to determine the source of the discrepancy.

Figure 35: ^{244}Cm and ^{245}Cm concentrations

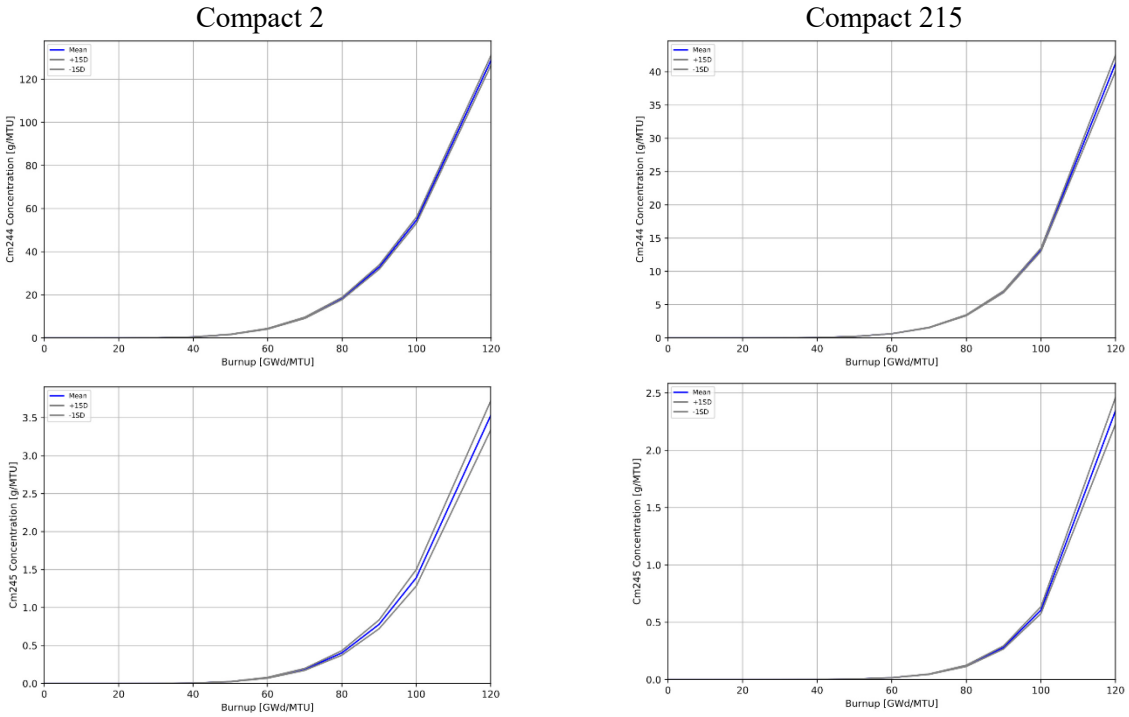

Source: OECD/NEA, 2020.

Figure 36: ^{241}Am concentrations

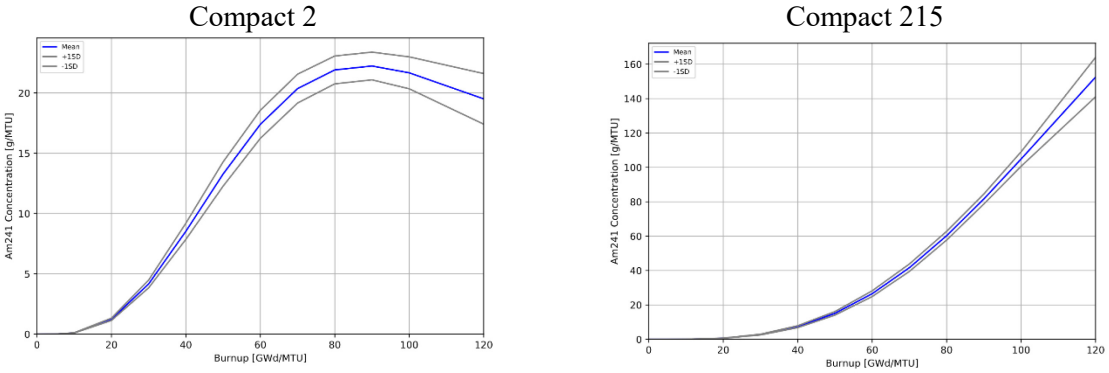

Source: OECD/NEA, 2020.

The ^{149}Sm and ^{151}Sm concentration are included in Figure 38 and show some variability between the codes. The differences stem from both HELIOS and MCCARD, which are further shown in Figures A8 and A9. Both isotopes are primarily produced through the fission of ^{235}U and higher actinides.

There is good agreement in the ^{90}Sr results shown in Figure 39, but the ^{137}Cs concentrations also show significant variation and are due to Serpent results. The values produced by Serpent are high through the depletion, which implies problems with fission yields for ^{137}Cs. Additional plots are provided in Figure A.10.

Finally, the results for ^{110m}Ag are shown in Figure 40 for HELIOS and DeCART because they were the only participants that tracked its production. There is approximately 20% difference in the final concentration of this isotope between the codes. The production of ^{110m}Ag is very important in HTGRs because ^{110m}Ag can migrate through the various TRISO particle layers. Unfortunately, not all computer codes include data for this isotope.

Figure 37: ^{135}Xe and ^{85}Kr concentrations

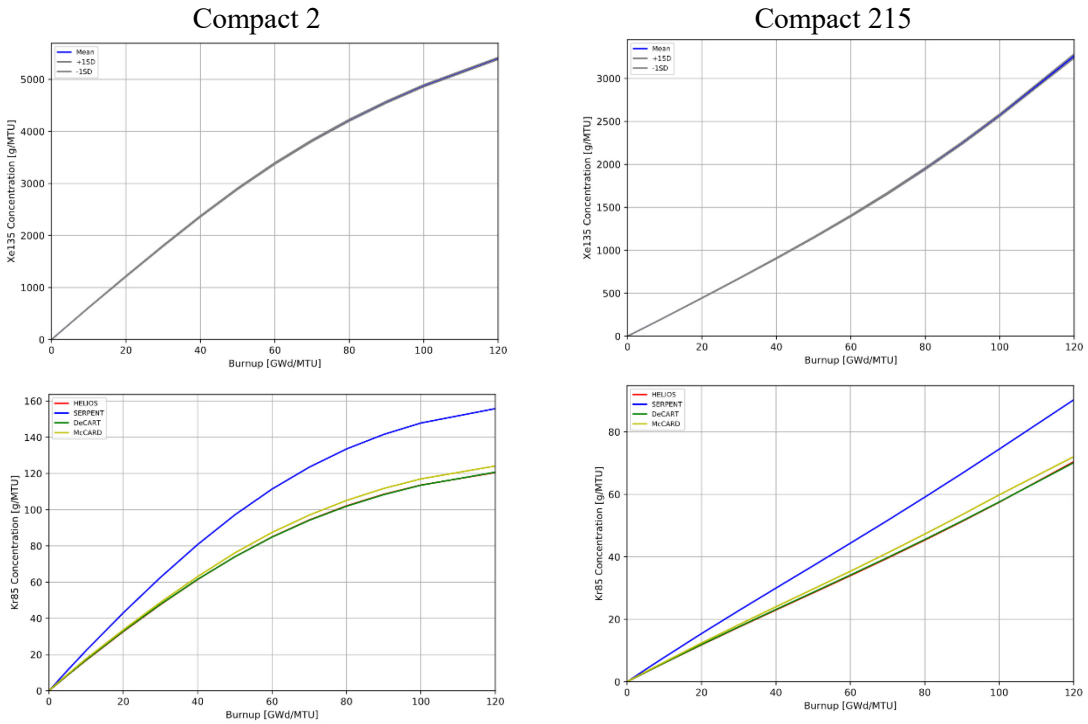

Source: OECD/NEA, 2020.

Figure 38: ^{149}Sm and ^{151}Sm concentrations

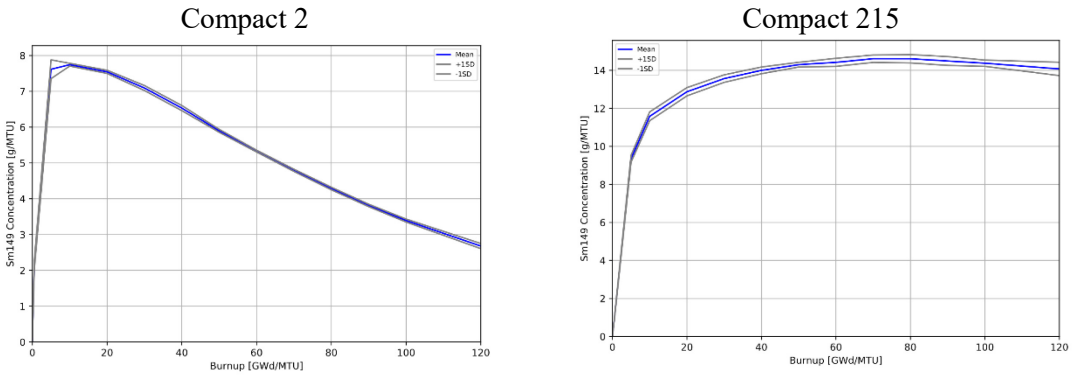

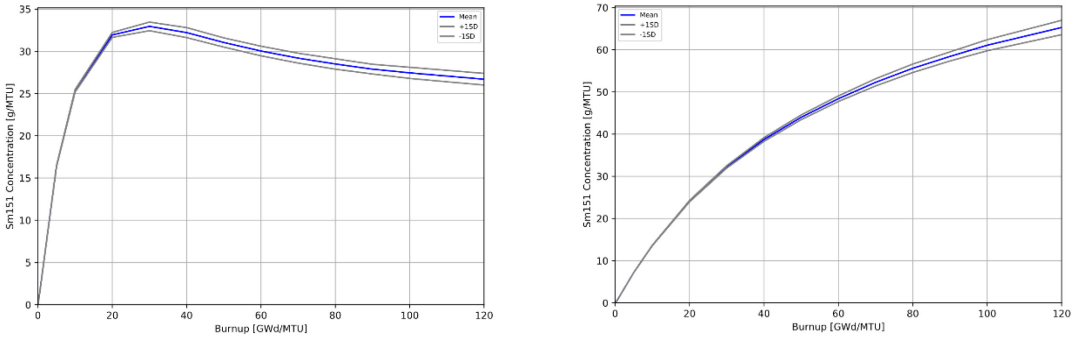

Source: OECD/NEA, 2020.

Figure 39: ^{137}Cs and ^{90}Sr concentrations

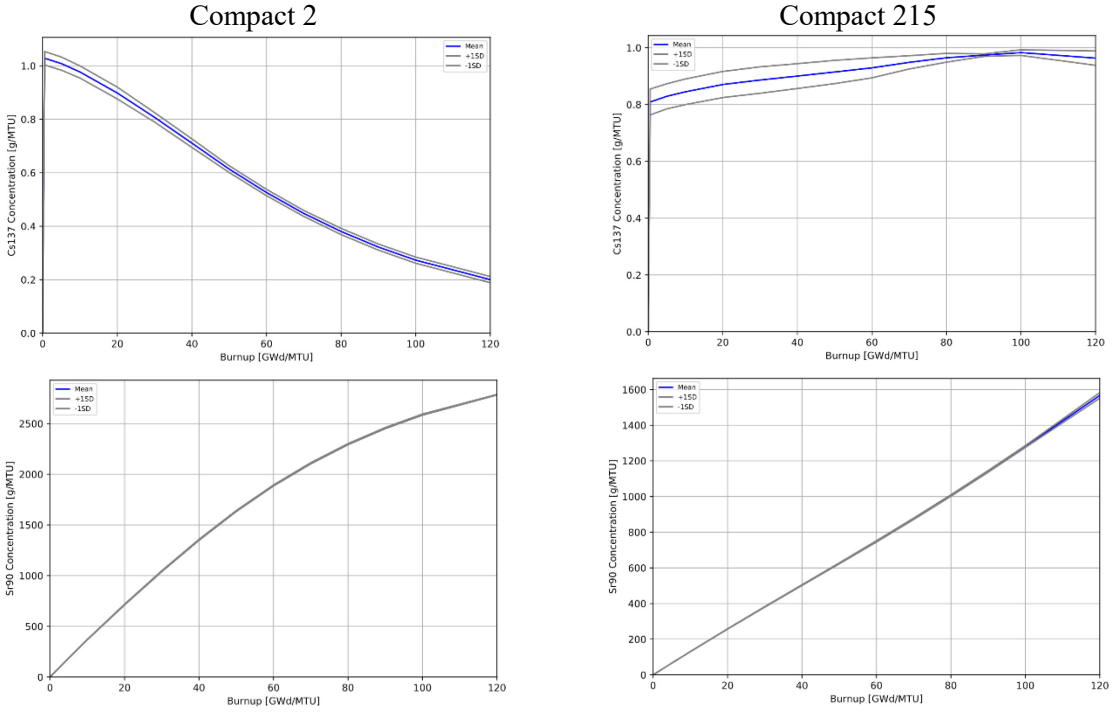

Source: OECD/NEA, 2020.

Figure 40: ^{110m}Ag concentrations

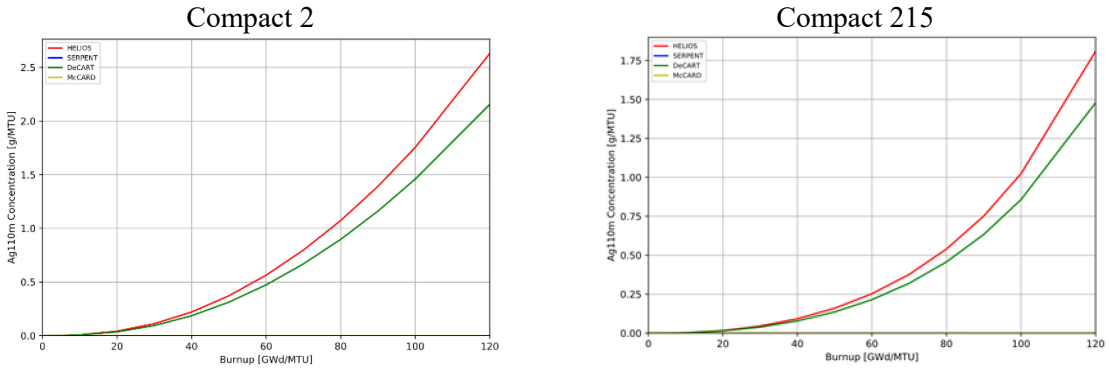

Source: OECD/NEA, 2020.

5. Conclusions

In this report, two exercises were performed to study the computational capabilities to predict neutronics characteristics of a MHTGR-350 supercell were undertaken. In the first exercise, the steady state room temperature neutronics predictions with and without burnable poisons were compared. While in the second exercise, the codes ability to predict depletion in both hot and cold conditions was tested.

Overall, results from the exercises show good agreement between the participants. In eigenvalue calculations for Exercise 1 and main depletion calculations for Exercise 2, the standard deviations are within 200 pcm. Temperature effect from 300 to 1 200 K is 4 385 and 5 553 pcm without and with burnable poisons (BPs), respectively. The BP worth is roughly -8%, which is consistent with other prismatic high-temperature gas reactor (HTGR) designs. There is good agreement among participants in predicting BP worth.

Significant initial flux and power gradient exist at beginning of life (BOL), with peaking factors ranging from 1.96 to 0.58 across the central fuel block in the cold case with BPs. Higher temperature tends to redistribute the power and reduce the power gradient, with peaking factors between 1.72 and 0.58. A consistency in the pattern of the results exists between the cold case, at 300 K, and the high-temperature case at 1 200 K. Peaking is much higher without BPs, with maximum values of 2.25 and 1.91 for the cold- and hot-temperature conditions, respectively. These gradients at BOL are ameliorated during the fuel burn-up, leading to power distributions that are quite constant across the central fuel block in comparison. There is good agreement in the compact peaking factors during the depletion, but agreement deteriorates slightly near end of life (EOL) for cases with and without BPs. All compact power distributions have standard deviations within 2.25%.

The central fuel block exhibits two well-defined neutron-energy-spectrum zones: a thermal-spectrum zone near the reflector region and a faster-spectrum zone near the burned-fuel region. Significant differences in the depletion of ^{235}U emerge between the two spectral zones, with the thermal zone undergoing four times more ^{235}U fissions than the hard-spectrum zone. The difference in ^{238}U depletion is roughly 10%, with ^{238}U depletion more prominent in the hard-spectrum zone. Peak production of ^{239}Pu is four times higher near the burned fuel due to the higher capture rate in ^{238}U.

The reactivity physical transformation (RPT) method performs well in the computation of integral parameters like reactivity and the BP worth, albeit with a significant varying bias. The RPT method does not track well the depletion of ^{238}U or the production of higher actinides. The ^{241}Am concentration is poorly predicted in Serpent during depletion. Other issues with fission-product production are observed in various codes, with ^{85}Kr being the largest source of discrepancy.

References

[1] Neylan, A.J., D.V. Graf, A.C. Millunzi (1988), "The modular high temperature gas-cooled reactor (MHTGR) in the US", *Nuclear Engineering and Design* 109, pp. 99–105.

[2] NEA (2015), "OECD/NEA Coupled Neutronic/Thermal-Fluids Benchmark of the MHTGR-350 MW Core Design, Volume III: Lattice Physics Exercises", www.oecd-nea.org/download/wprs-mhtgr/documents/MHTGR-350-Vol_III-Benchmark_Lattice.r0.pdf (working document with restricted access).

[3] Sanchez, R., G.C. Pomraning (1991), "A statistical analysis of the double heterogeneity problem", *Annals of Nuclear Energy* 18.7, pp. 371–395, ISSN 0306-4549, DOI: 10.1016/0306-4549(91)90073-7.

[4] Sanchez, R., E. Masiello (2002), "Treatment of the double heterogeneity with the method of characteristics", *Proceedings of PHYSOR–2002, held in Seoul, Korea, 7-10 October 2002*.

[5] Kim, Y. et al. (2005), "Elimination of double-heterogeneity through a reactivity-equivalent physical transformation", *GLOBAL 2005, held in Tsukuba, Japan, 9-13 October 2005*.

[6] Rohde, U., S. Baier, S. Duerigen, E. Fridman, S. Kliem, and B. Merk (2011), "Development and verification of the coupled 3D neutron kinetics/thermal-hydraulics code DYN3D-HTR for the simulation of transients in block-type HTGR", *Nuclear Engineering and Design* 251, pp. 412-422, DOI:101016/jnucengdes201109051.

[7] Miloševtć, M.J. (1998), "A subgroup method for resonance interference factor calculation", YUNSC 98−2*nd International Yugoslav Nuclear Society Conference, held in Belgrade, Yugoslavia, 28 September-1 October 1998.*

Bibliography

Duderstadt, J.J. and L. J. Hamilton (1976), *Nuclear Reactor Analysis*, 1st ed., John Wiley & Sons, New Jersey.

Massimo, Luigi (1976), *Physics of High-temperature Reactors*, 1st ed., Pergamon Press, Oxford.

Annex A: Supporting plots for Exercise 2

Figure A.1: ^{238}U depletion for case 2b

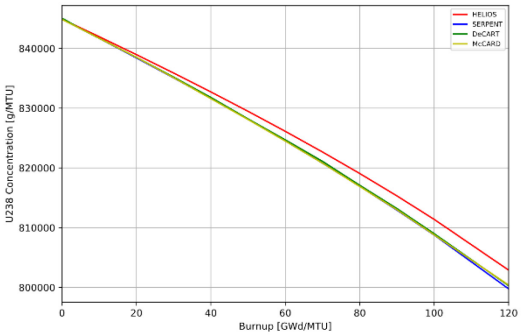

Compact 2

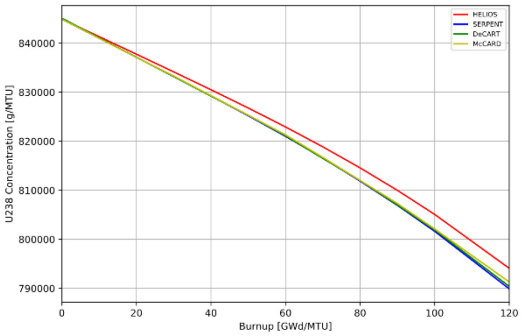

Compact 215

Source: OECD/NEA, 2020.

Figure A.2: ^{239}Pu depletion for case 2b

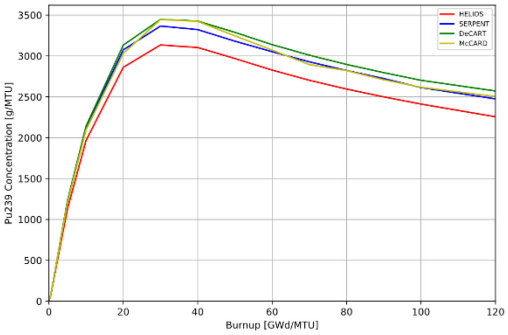

Compact 2

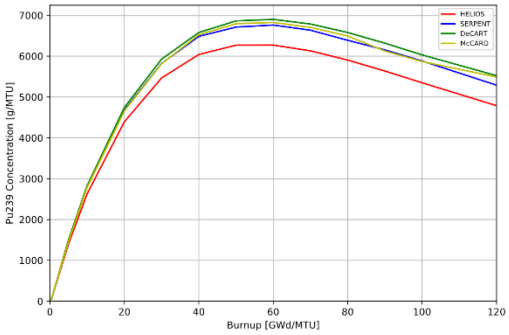

Compact 84

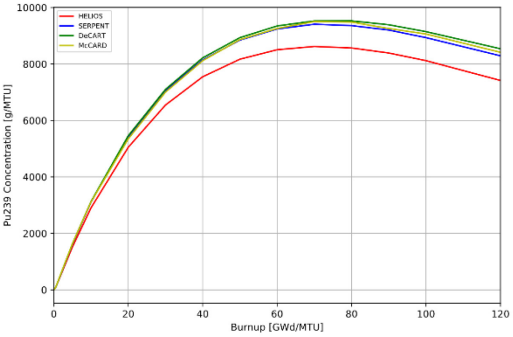

Compact 133

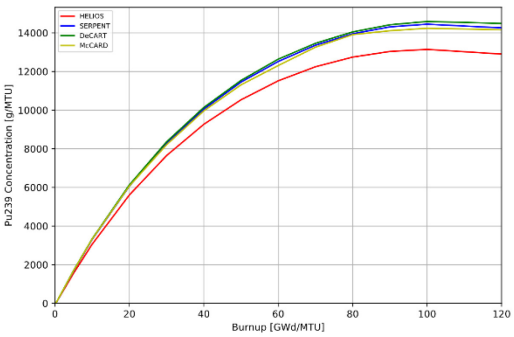

Compact 215

Source: OECD/NEA, 2020.

Figure A.3: ^{240}Pu concentrations for case 2b

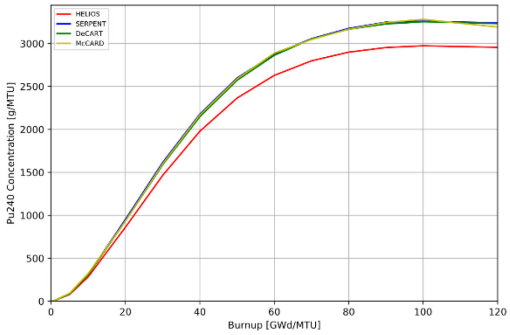

Compact 2

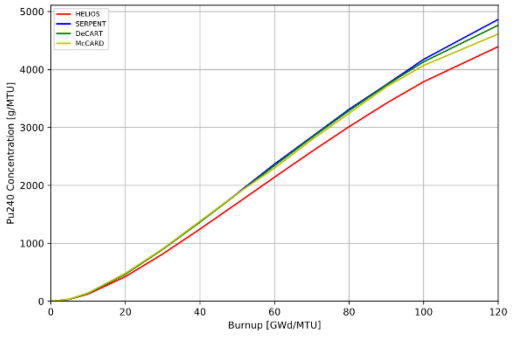

Compact 215

Source: OECD/NEA, 2020.

Figure A.4: ^{241}Pu concentrations for case 2b

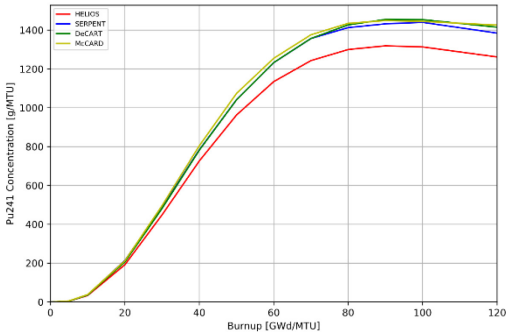

Compact 2

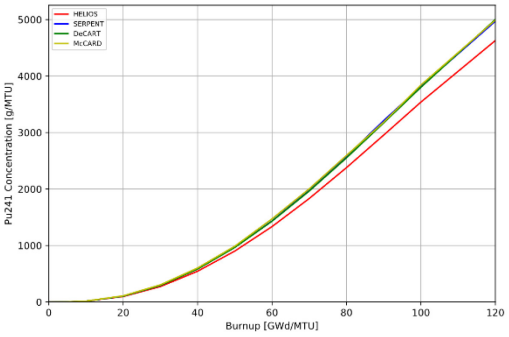

Compact 215

Source: OECD/NEA, 2020.

Figure A.5: ^{242}Pu concentrations for case 2b

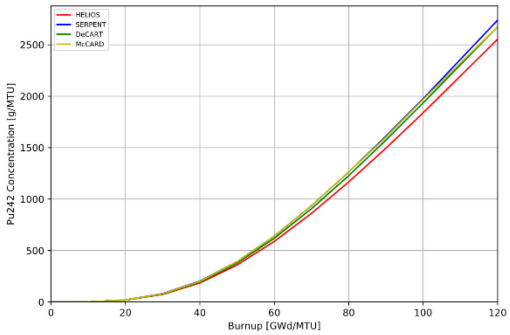

Compact 2

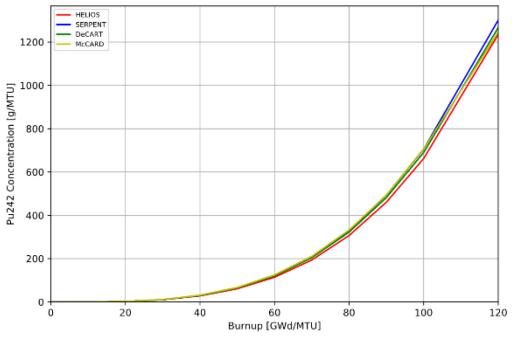

Compact 215

Source: OECD/NEA, 2020.

Figure A.6: ^{245}Cm concentrations for case 2b

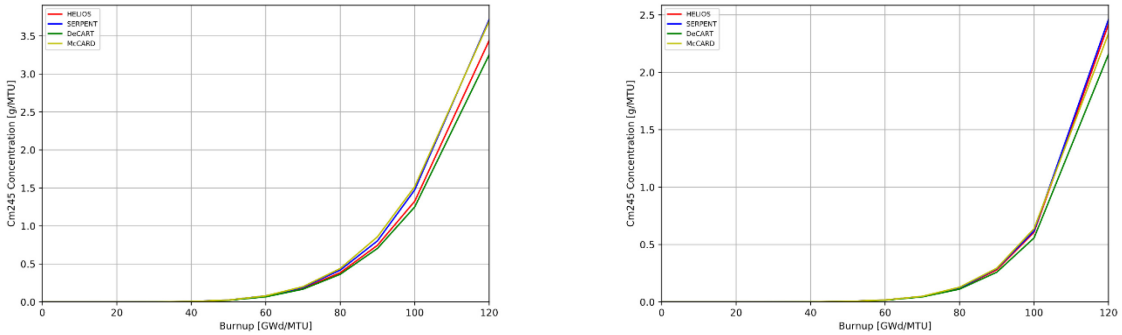

Compact 2 Compact 215

Source: OECD/NEA, 2020.

Figure A.7: ^{241}Am concentrations for case 2b

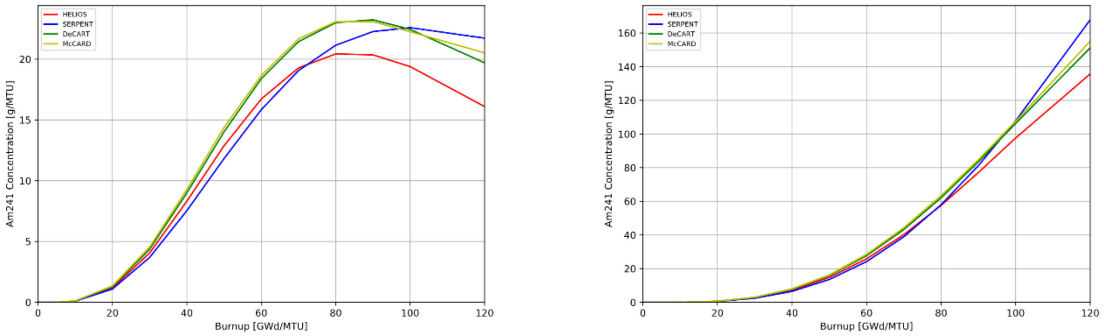

Compact 2 Compact 215

Source: OECD/NEA, 2020.

Figure A.8: ^{149}Sm concentrations for case 2b.

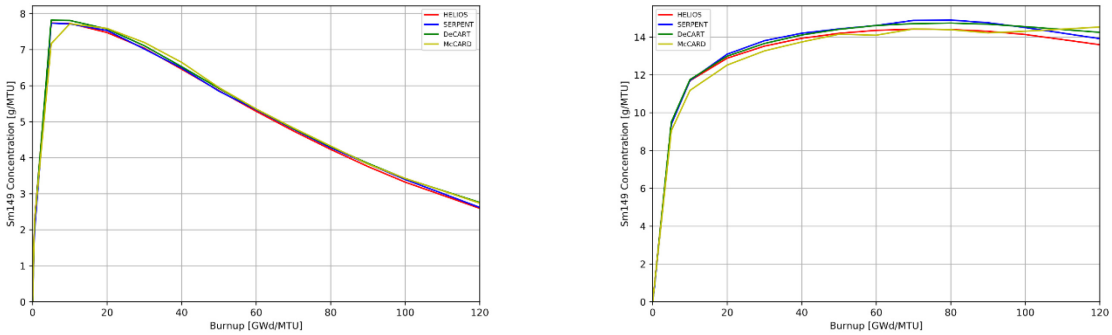

Compact 2 Compact 215

Source: OECD/NEA, 2020.

Figure A.9: ^{151}Sm concentrations for case 2b

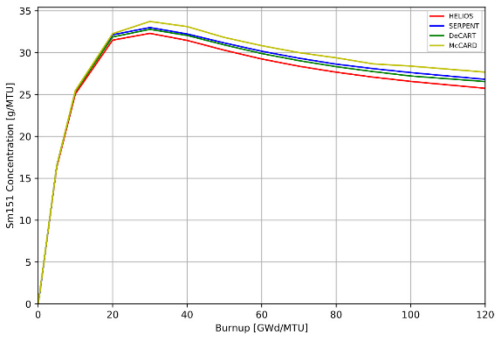

Compact 2

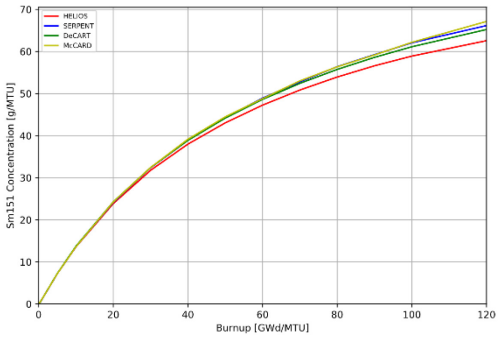

Compact 215

Source: OECD/NEA, 2020.

Figure A.10: ^{137}Cs concentrations for case 2b

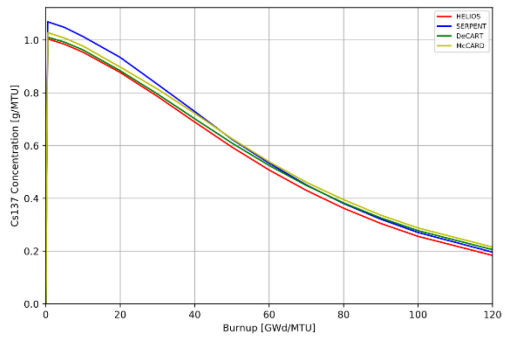

Compact 2

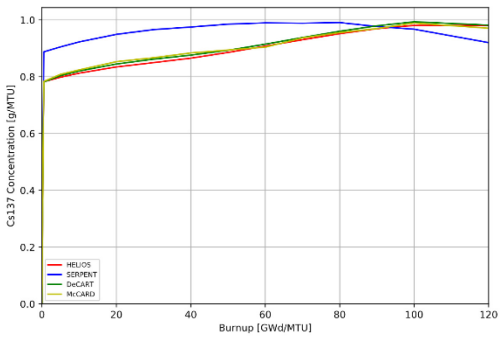

Compact 215

Source: OECD/NEA, 2020.

Annex B: List of participants

1. **Idaho National Laboratory (INL), United States**
   Participant: Javier Ortensi
   Code(s): Serpent 2

2. **Korea Atomic Energy Research Institute (KAERI), Korea**
   Participants: Tae Young Han, Hyun Chul Lee
   Code(s): DeCART, McCARD

3. **Gesellschaft für Anlagen- und Reaktorsicherheit (GRS), Germany**
   Participants: Armin Seubert in collaboration with Javier Ortensi (INL)
   Code(s): Helios 2